J. Fluid Mech. (2011), *vol.* 671, *pp.* 254–287. © Cambridge University Press 2011
doi:10.1017/S0022112010005604

Three-dimensional interactions between a finite-span synthetic jet and a crossflow

ONKAR SAHNI[1]†, JOSHUA WOOD[2], KENNETH E. JANSEN[3] AND MICHAEL AMITAY[2]‡

[1]Scientific Computation Research Center, Rensselaer Polytechnic Institute, Troy, NY 12180, USA

[2]Mechanical, Aerospace and Nuclear Engineering Department, Rensselaer Polytechnic Institute, Troy, NY 12180, USA

[3]Aerospace Engineering Sciences, University of Colorado, Boulder, CO 80309, USA

(Received 18 March 2010; revised 9 September 2010; accepted 19 October 2010; first published online 9 February 2011)

A complementary experimental and numerical investigation was performed to study the three-dimensional flow structures and interactions of a finite-span synthetic jet in a crossflow at a chord-based Reynolds number of 100 000 and a 0° angle of attack. Six blowing ratios in the range of 0.2–1.2 were considered. Experiments were conducted on a finite wing with a cross-sectional profile of NACA 4421, where particle-image velocimetry data were collected at the centre jet. To complement the experiments, three-dimensional numerical simulations were performed, where the numerical set-up matched not only the physical parameters (e.g. free stream) but also the physical dimensions (e.g. orientation and location of the jet. For the low blowing ratio cases, spatial non-uniformities developed, due to the finite span of the slit, which led to the formation of small and organized secondary structures or a streak-like pattern in the mean flow. On the other hand, for the high blowing ratio range, turbulent vortical structures were dominant, leading to larger spanwise structures, with a larger spanwise wavelength. Moreover, the phase-locked flow fields exhibited a train of counter-rotating coherent vortices that lifted off the surface as they advected downstream. In the mid-blowing ratio range, combined features of the low range (near the slit) and high range (in downstream locations) were found, where a pair of counter-rotating vortices issued in the same jet cycle collided with each other. In all cases, the spanwise extent of the secondary coherent structures reduced with downstream distance with a larger decrease at higher blowing ratios. Similar observations were made in earlier studies on finite-span synthetic jets in quiescent conditions.

Key words: flow control, instability control

1. Introduction

The major goal in aerodynamics is to improve vehicle performance over a wide range of operating conditions. This can be achieved by optimizing the shape or by using passive and/or active flow control techniques. Active flow control techniques

† Present address: Center for Predictive Engineering and Computational Sciences, Institute for Computational Engineering and Sciences, The University of Texas at Austin, Austin, TX 78712, USA.

‡ Email address for correspondence: amitam@rpi.edu

https://doi.org/10.1017/S0022112010005604 Published online by Cambridge University Press

based on fluidic actuators have been widely studied and used due to their dynamic applicability over a broad range of flow conditions along with their efficiency (e.g. separation mitigation at high angles of attack and virtual aero-shaping at low angles of attack). One approach is to couple the actuation frequency to instabilities inherent to separated flows and thus alter the global flow field by modifying the large-scale vortical structures (e.g. Oster & Wygnanski 1982; Ho & Huerre 1984; Roberts 1985; Seifert *et al.* 1993; Wygnanski 2000). In this approach, the time period of actuation scales with the advection time through the length of the flow domain downstream of the separation (as measured by the reduced or non-dimensional frequency, F^+). In such an approach, control input is effective within a limited spatial domain immediately upstream of separation; however, when the flow is not separated (e.g. at low angles of attack), the efficacy of this approach is negligible (e.g. Seifert *et al.* 1993).

A different approach, in which fluidic actuators that are driven at much larger frequencies than characteristic flow frequencies (such as synthetic jets: e.g. Amitay & Glezer 2002*a*; Glezer, Amitay & Honohan 2005), allows more control through the modification of the apparent aerodynamic shape of the lifting surfaces (e.g. Amitay *et al.* 1997, 2001*b*). This approach does not necessarily rely on coupling the actuation frequency to global flow instabilities and can therefore be applied to various spatial locations and over a broader range of flow conditions (e.g. Amitay *et al.* 2001*a*; Glezer & Amitay 2002). Furthermore, it can accommodate a broader band control algorithms where more complex actuation waveforms can be used (e.g. the pulse modulation technique, Amitay & Glezer 2006).

In the last decade, a variety of promising flow control applications based on synthetic jet actuators have been presented. Several studies on synthetic jet applications have demonstrated that flow separation can be mitigated or even suppressed altogether (e.g. see Amitay *et al.* 1999; Crook, Sadri & Wood 1999; He, Cary & Peters 2001; Amitay & Glezer 2002*b*). Synthetic jets have also been used for separation control in inlet ducts (e.g. Amitay, Pitt and Glezer 2002*c*). It has also been demonstrated on unmanned aerial vehicles (e.g. Parekh *et al.* 2003) and jet vectoring (e.g. Smith & Glezer 2002), as well as for flight control on scaled models (e.g. Ciuryla *et al.* 2007). More recently, it has been used for vibration suppression in wind turbines by Maldonado *et al.* (2010). Synthetic jets have also been applied at low angles of attack, where the flow is fully attached, for two-dimensional (2-D) platforms (e.g. Chatlynne *et al.* 2001; Amitay *et al.* 2001*a*) and also for three-dimensional (3-D) configurations (e.g. Farnsworth *et al.* 2008). In some studies, significant control forces were imparted by cropping the trailing edge of an aerofoil and using synthetic jets (e.g. Timor *et al.* 2007), which indicates an opportunity to replace the conventional control surfaces (e.g. flaps, aileron and rudder) with active flow control, or at least augment their performance in terms of control authority as well as frequency response.

Apart from such attractive synthetic jet-based flow control applications, a large number of studies have been performed to investigate and characterize the flow structures and mechanisms due to synthetic jet actuation. These studies were experimental, computational or combined. More importantly, these investigations can be classified into two broad classes: (*a*) synthetic jets in quiescent conditions and (*b*) synthetic jets in a crossflow. Furthermore, these studies involved synthetic jets that were issued through orifices of different geometry ranging between (i) plane 2-D or very-high-aspect-ratio slits, minimizing the end effects (i.e. with aspect ratios of 75 or above); (ii) circular, elliptic or low-aspect-ratio slits (with aspect ratios below 5); and

https://doi.org/10.1017/S0022112010005604 Published online by Cambridge University Press

(iii) finite-span or rectangular slits with end effects (i.e. with aspect ratios between 5 and 75). Therefore, in this section, three categories are considered and discussed, namely (i) synthetic jets in quiescent conditions (including circular, elliptic or rectangular slits covering the full range of aspect ratios), (ii) low-aspect-ratio synthetic jets in a crossflow and (iii) finite-span rectangular synthetic jets in a crossflow. The rationale for this categorization is that the majority of the existing studies, to the best of the authors' knowledge, lie in the realm of the first two categories. On the other hand, flow structures formed due to the finite span of rectangular synthetic jets can play an important role in various flow control applications (e.g. separation control and virtual aero-shaping) and require a deeper understanding; therefore, it is the focus of the present work.

1.1. *Synthetic jets in quiescent conditions*

Smith & Glezer (1998) were the first to experimentally study the flow field of a synthetic jet in quiescent conditions (i.e. without a crossflow). In their study, the jet was issued via a rectangular slit of a very high aspect ratio (i.e. 150). They showed, using spanwise flow visualization along the long axis of the slit, that periodically formed discrete vortex pairs undergo a transition to turbulence in a jet cycle and lose their coherence due to formation of instabilities in the form of spanwise-regular rib-like secondary vortical structures.

Numerical investigations of synthetic jets in quiescent conditions were performed by Kral *et al.* (1997) and Lee & Goldstein (2002) based on 2-D simulations, while Rizzetta, Stanek & Visbal (1999) performed high-resolution 3-D simulations. Note that in the 3-D simulations of Rizzetta *et al.* (1999), the spanwise length of the slit was reduced by a factor of 10 as compared with the experiments of Smith & Glezer (1998) and, furthermore, symmetry conditions at the jet centreline and mid-span were used to include only one quarter of the physical configuration. This was done due to limitation on computing resources. Two-dimensional simulations agreed with the experiments near the exit of the jets where the flow field was dominated by counter-rotating vortex pairs, while farther away from the jet slit (i.e. after 10 slit widths) there was significant disagreement. On the other hand, 3-D simulations (by Rizzetta *et al.* 1999) captured spanwise instabilities, which led the counter-rotating vortex pair to lose their coherence and break down farther downstream, as was observed in the experiments (even though it was not possible in 3-D simulations to exactly duplicate the experimental configuration in terms of the spanwise length of the jet slit). Mallinson, Hong & Reizes (1999), Crook & Wood (2001), Cater & Soria (2002) and Zaman & Milanovic (2003) also made similar observations on 3-D flow structures and instabilities for synthetic jets issued through a circular orifice.

More recently, Yao *et al.* (2004) conducted detailed experimental measurements of synthetic jets in quiescent conditions to be used for validation studies. The synthetic jet in this case had a rectangular slit with an aspect ratio of 28. Measurements were made using three different techniques, namely particle image velocimetry (PIV), laser Doppler velocimetry (LDV) and hot-wire anemometry, which included both near- and far-field measurements as well as measurements on two planes along and across the slit. Yao *et al.* (2004) showed that besides the end effects at the edge of the jet slit, 3-D flow structures develop due to spanwise instabilities when the jet is advected downstream. They noted, as was done by Smith & Glezer (1998), that near the jet slit, flow behaviour is relatively smooth and uniform, while the jet front develops wavy profiles downstream.

https://doi.org/10.1017/S0022112010005604 Published online by Cambridge University Press

Numerical investigations for this case were done with varying degrees of success, which were based on 2-D and 3-D simulations. As before, in contrast to 2-D simulations, high-resolution 3-D simulations were able to capture spanwise instabilities in the form of rib-like secondary structures in the primary vortex pair (see Kotapati, Mittal & Cattafesta 2007: they did not model the end effects by considering a jet along the entire span of the computational domain). Cui & Agarwal (2006) also performed 3-D simulations and included slot ends but showed limited agreement with the experiments, possibly because the grid used was fairly coarse with only 29 points along the spanwise length of the slit (note that the aspect ratio of the slit is 28). For a detailed survey of simulations for this case, see Rumsey (2009).

Amitay & Cannelle (2006) also carried out detailed experimental measurements for finite-span synthetic jets (i.e. issued via rectangular slits) in quiescent conditions, where they collected PIV data on two planes across and along the slit. They considered a range of orifice aspect ratios (from 50.8 to 101.6) and synthetic jet parameters (including stroke length and actuation frequency). As in earlier studies, they showed that vortex pairs near the jet orifice are uniform and two-dimensional but farther downstream develop horseshoe-like patterns, with secondary counter-rotating vortical structures along the span that form an array of streaks in the mean flow. They also showed the presence of edge-induced vortices due to the finite span of the slit as well as 3-D instabilities that prevail in the mid-span of the jet (even for a case with an aspect ratio of 101.6, as was visualized by Smith & Glezer 1998). Cannelle & Amitay (2007) extended these studies to investigate the transitory behaviour of synthetic jets (following the onset and termination of the actuation), where they also made hot-wire measurements and showed the formation, evolution and merging of vortices in the cross-stream and spanwise planes.

1.2. *Low-aspect-ratio synthetic jets in a crossflow*

In addition to detailed investigations of synthetic jets issued into a quiescent flow, the second category of studies involves synthetic jets in a crossflow. Such studies, leading to understanding and characterization of flow structures and interactions due to synthetic jet actuation in the crossflow, are critical for their effective application in flow environments of practical interest. Most of the studies on synthetic jets in a crossflow have considered circular or elliptic orifices (with low aspect ratio). Crook & Wood (2001) used a water tunnel and studied an isolated circular synthetic jet in a crossflow along with an array of synthetic jets on a tripped circular cylinder. In their experiments, they used dye visualization to show the 3-D interactions of vortical structures due to their tilting, stretching and mutual interaction. Similarly, Sauerwein & Vakili (1999) studied 3-D interactions of vortex rings for several synthetic jet configurations in a water tunnel. Gordon & Soria (2002) also used a water tunnel and carried out PIV measurements for a circular synthetic jet in a crossflow. They considered only one measurement plane located at the centre of the orifice and aligned with the crossflow. On the basis of these PIV data, they observed deflection in the mean streamlines of the crossflow to be up to 2–3 orifice diameters from the wall and for a distance up to 15–20 diameters.

Zaman & Milanovic (2003) used hot-wire anemometry in wind-tunnel experiments to study a circular synthetic jet in a turbulent boundary layer and showed the formation of a counter-rotating vortex pair, a region of low momentum downstream of the jet (due to the blockage caused by the jet), and also high turbulence intensity regions. Milanovic & Zaman (2003) further extended their investigation to orifices of different geometries, including straight, tapered, pitched and clustered jet slots,

https://doi.org/10.1017/S0022112010005604 Published online by Cambridge University Press

all with the same cross-section at the slit. For the most part, they observed similar flow structures between different orifices. The differences were in the jet penetration, which was somewhat smaller in the case of pitched and clustered orifices, and as expected, the pitched jet also led to a region of high momentum near the wall. In another study, Milanovic, Zaman & Rumsey (2005) carried out a joint experimental and computational investigation of a straight circular synthetic jet in a crossflow. They showed the overall agreement to be good in both axial and transverse planes but computational results overpredicted the extent of the velocity deficit regions.

Schaeffler & Jenkin (2006) carried out detailed measurements, including LDV as well as planar and stereoscopic PIV, for a circular synthetic jet in a turbulent crossflow to be used as a validation database (similar to the case of a synthetic jet in quiescent conditions by Yao *et al.* 2004). They showed the same features of deflection in the mean streamlines of the crossflow in the axial symmetry plane and counter-rotating vortex pair in the transverse plane. As before, follow-up numerical studies, including 2-D and 3-D simulations, were carried out for this case. Three-dimensional simulations showed reasonable qualitative agreement with experiments (e.g. see Cui & Agarwal 2005; Xia & Qin 2005; Dandois, Garnier & Sagaut 2006); for a survey of numerical simulations for this case, see Rumsey (2009).

Other detailed experimental studies on circular synthetic jets in a crossflow were carried out recently by Jabbal & Zhong (2008) and Iai, Motosuke & Honami (2009), all of which were conducted in a laminar or a low-Reynolds-number crossflow. Jabbal & Zhong (2008) used a water tunnel to investigate the flow field of a circular synthetic jet on a flat plate. They carried out measurements based on stereoscopic dye visualization and thermochromic liquid crystal-based convective heat transfer sensing system to detect thermal footprints of passing flow structures. They identified three different types of vortical structures based on the range of blowing ratio, namely hairpin vortices, stretched vortex rings and tilted/distorted vortex rings. Furthermore, on the basis of the thermal footprints of the flow structures, they conjectured that either hairpin vortices or stretched vortex rings were responsible for the delayed separation on the circular cylinder studied by Crook & Wood (2001). The study of Iai *et al.* (2009) was carried out in a fully developed low-Reynolds-number channel flow, which included a circular synthetic jet oriented either perpendicular to the crossflow or with a 45° pitch. Their measurements were based on a scanning stereoscopic PIV system with multiple planes along the span to construct a 3-D flow field (similar to the technique used in the present study). One blowing ratio for both configurations of the synthetic jet was considered and formation of hairpin vortex structure was observed. As expected, in the inclined configuration, asymmetry existed in the two longitudinal vortices of the hairpin structure.

More validation studies on the interaction of circular synthetic jets with a crossflow include Zhou & Zhong (2009) and Wu & Leschziner (2009). Zhou & Zhong (2009) showed good agreement with the laminar case of Jabbal & Zhong (2008), whereas Wu & Leschziner (2009) considered a turbulent crossflow over a flat plate and showed reasonably good agreement at downstream locations. Numerical studies were also carried out ranging from 2-D to 3-D simulations. For example, Mittal, Rampunggoon & Udaykumar (2001) and Mittal & Rampunggoon (2002) performed 2-D simulations of synthetic jets in a laminar flow over a flat plate and showed the existence of recirculation bubbles in the mean flow near the orifice to demonstrate the virtual aero-shaping effect, whereas Ravi, Mittal & Najjar (2004) investigated effects of square and rectangular orifices (with an aspect ratio up to 4) based on 3-D simulations; however, they presented limited results due to constraints on computing resources.

https://doi.org/10.1017/S0022112010005604 Published online by Cambridge University Press

1.3. *Finite-span rectangular synthetic jets in a crossflow*

Smith (2002) performed wind-tunnel experiments on an array of finite-span synthetic jets in a turbulent boundary layer (each jet had a rectangular orifice with an aspect ratio of 45). Two configurations of three parallel synthetic jets aligned in the spanwise and streamwise directions on a flat plate were considered. All the measurements were based on hot-wire anemometry, and therefore it was noted that understanding 3-D flow structures in detail was difficult. Nevertheless, prominent features were shown, for example, spanwise configuration with an orifice normal to the crossflow showed that the blockage was caused just upstream of the orifice along with a wake-like feature in the downstream region. Moreover, the orifice aligned in the streamwise direction exhibited longitudinal vortices embedded in the boundary layer.

Gilarranz, Traub & Rediniotis (2005) also carried out wind-tunnel experiments on finite-span synthetic jets (with an aspect ratio of 22.35) over a NACA 0015 wing with an aspect ratio of about 1 (end plates were used to minimize the 3-D effects due to finite span of the wing). They considered a high Reynolds number (i.e. 890 000) and varied the angle of attack from low to high (i.e. -2° to 29°). Their results were based on force balance measurements, on-surface oil flow visualization, smoke flow visualization, surface pressure measurements and wake surveys. On the basis of these measurements, they showed significant effects due to synthetic jet actuation at high angles of attack, where the onset of stall was delayed from 12° to 18°, and up to 80 % increase in the lift coefficient was observed. They also showed a decrease in drag due to synthetic jet actuation. Recently, You & Moin (2008) numerically simulated this case at the same Reynolds number and at an angle of attack of 16.6°. In their 3-D simulations, they considered the jet slit to cover the entire span of the computational domain, thus eliminating the end effects. They showed good agreement for the lift coefficient and the wake. Furthermore, they presented phase-averaged velocity profiles, streamlines and pressure field, as well as instantaneous iso-surfaces of vorticity, which helped in understanding the interaction of the jet with the crossflow but without any end effects.

The motivation behind the present paper is to extend the understanding of the interaction of a finite-span synthetic jet with a crossflow, specifically to investigate and explore the formation and evolution of secondary flow structures in the vicinity of the jet. In the current case, a low chord-based Reynolds number of 100 000 and a 0° angle of attack were selected. Also, note that the jet was located near the leading edge at 17 % of the chord (i.e. near the suction peak). Thus, the synthetic jet experienced a crossflow with an oncoming boundary layer that was attached and laminar as it developed over the aerofoil in a region with a strong favourable pressure gradient. Nevertheless, flow structures due to the synthetic jet at high blowing ratio cases were found to be turbulent in downstream locations (as also seen without a crossflow; e.g. Smith & Glezer 1998; Rizzetta *et al.* 1999; Amitay & Cannelle 2006).

Complementary experimental and numerical studies were performed, where 2-D and stereoscopic PIV experimental measurements were carried out in the near vicinity of the synthetic jet for six different blowing ratios, whereas high-resolution numerical simulations were performed for two blowing ratios (one in the lower range and the other in the higher range). The resolution used in the current numerical simulations was adequate to resolve the physical scales well into the dissipation range in the vicinity of the jet, i.e. within the interrogation domain of interest, direct numerical simulation (DNS) was applied, while far outside the interrogation domain the mesh resolution was coarsened to one that is more typically used for large-eddy simulation

https://doi.org/10.1017/S0022112010005604 Published online by Cambridge University Press

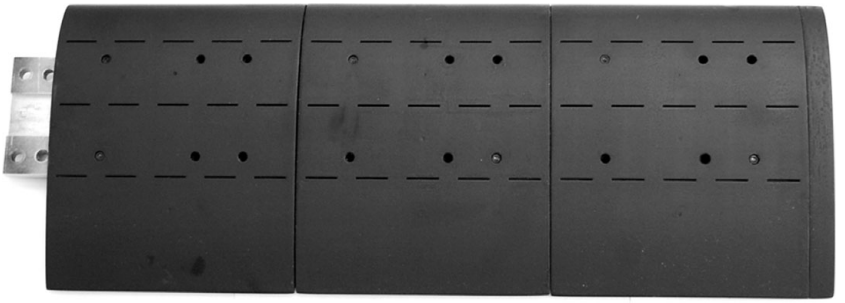


FIGURE 1. Picture of the wind-tunnel model with three modules of synthetic jets along the span.

(LES). Note that upstream of the jet, the flow is laminar and transition is therefore captured with DNS resolution within the interrogation domain of interest that allows high confidence in the numerical simulation. Stabilized finite-element methods such as the one used here have been shown to be capable of handling both LES and DNS accurately (e.g. see Bazilevs *et al.* 2007; Trofimova *et al.* 2009). The primary focus of the current joint investigation was to provide a detailed and complementary understanding of the flow interaction, specifically in the vicinity of the synthetic jet, and as a necessary step to validate both techniques. One of the advantages of this complementary work includes availability of instantaneous and detailed 3-D flow fields (which are readily available from simulations) as well as long-time averaged fields (including both time-averaged or phase-averaged fields, which are easier to obtain from experiments). The broad goal of this ongoing work is to understand the flow mechanisms associated with an array of synthetic jet actuators over true 3-D platforms (e.g. finite wings with sweep and/or taper). This knowledge can then be used to efficiently implement active flow control for flight control in lieu of, or in addition to, conventional control surfaces.

This paper is organized as follows. Sections 2 and 3 describe the experimental and numerical set-up and procedures, respectively. Section 4 discusses the results covering the quasi-periodic flow behaviour along the mid-span (in § 4.1), time-averaged flow field (in § 4.2) and instantaneous and phase-averaged flow fields (in § 4.3). Conclusions are presented in § 5.

2. Experimental set-up

The experiments were conducted in an open-return wind tunnel at Rensselaer Polytechnic Institute, where the test section has a cross-section of 80 cm × 80 cm and is 457 cm long. The model used in the experiments was a finite wing with a constant chord, $c = 15.24$ cm, and a span of $b = 40.64$ cm (resulting in an aspect ratio of 5.33), and a cross-sectional shape of NACA 4421 aerofoil (see Abbott & von Doenhoff 1959). A thick aerofoil was selected such that it can be instrumented with multiple synthetic jet actuators. The model was divided into three sections along the span; each section was instrumented with 15 synthetic jet actuators organized in three rows (figure 1). Only the first row of jets was considered in the present study, which was centred at about 17 % of the chord (from the leading edge). The spanwise spacing between side edges of subsequent jets in each row is 5.4 mm. All jet orifices were oriented perpendicular to the surface and had a length of $L_z = 16$ mm (along the

https://doi.org/10.1017/S0022112010005604 Published online by Cambridge University Press

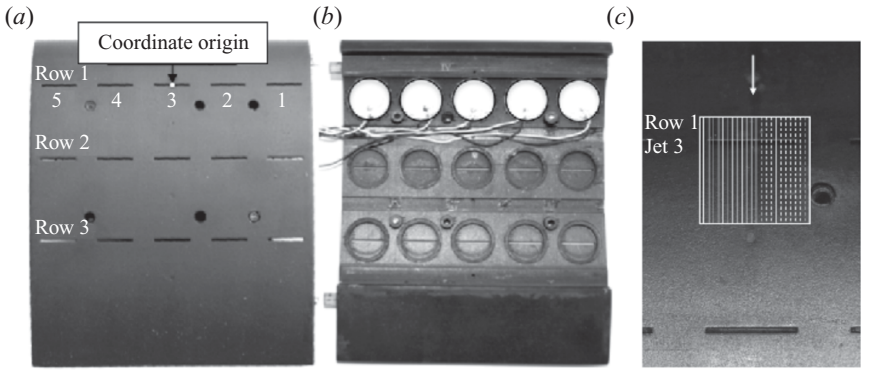


FIGURE 2. Picture of the centre module, with three rows of jets and five jets in each row, front side (*a*) and back side (*b*). (*c*) PIV measurement planes at jet 3. Solid lines represent planes on which data were acquired, while dashed lines are the symmetry planes.

span) and a width of $h = 0.75$ mm (in the streamwise direction), leading to an aspect ratio of 21.33. Each jet consisted of a discrete cavity and a 20 mm diameter single piezoelectric disk that was mounted on the side opposite the orifice (figure 2). Each jet slot had a height of 3 mm and was connected to a cavity chamber of a 3 mm height and a radius of 8.75 mm. The disk (from Murata, model number 7BB-20-3) was made of a piezoelectric material attached to a Brass substrate and had a resonance frequency of 3 600 Hz.

The three model sections (made by stereolithography) were attached to an aluminium skeleton. In addition, a circular fence (203.2 mm in diameter) was placed at the root of the wing to isolate the model from the tunnel wall boundary layer. The wing assembly was attached to a motor-driven pitch mechanism to enable a precise control of the angle of attack. The control of the angle of attack was achieved by a belted motor and an optical encoder that ensured the accuracy of the angle of attack to $\pm 0.1^{\circ}$. The entire assembly was mounted in upside-down configuration on one of the sidewalls of the wind tunnel to allow the NG-YAG laser for the PIV system to issue from below the tunnel, as the top of the tunnel is not optically accessible. Charge-coupled-device (CCD) cameras were mounted on an optical table, one for the 2-D PIV and two for stereoscopic PIV. The cameras were aligned perpendicular to the laser light sheet to allow for streamwise planes to be acquired.

The PIV system used is a commercial LaVision system of hardware and software including two 120 mJ Nd:YAG lasers and two 1376×1040 pixel resolution thermo-electrically cooled 12 bit CCD cameras. A cylindrical lens with a focal length of 50 mm was used to create the light sheet and a focal lens (with a focal length range of 500 to 1500 mm) was used to focus the sheet at the measurement domain (the thickness of the light sheet at the centre of the measurement domain was about 1 mm). The laser light sheet was then aligned with the area of interest using a computer-controlled three-axis traversing system mounted below the test section. The flow was seeded with $O(1\,\mu\text{m})$ water-based smoke particles, generated by a theatrical fog machine. The flow field was imaged using the CCD cameras mounted on their own independently controlled three-axis traverse. The velocity components (U, V, W) were computed from the cross-correlation of pairs of successive images with 50 % overlap between the interrogation domains. The images were processed using an advanced multi-pass method, where the initial and final correlation passes were 64×64 and 16×16 pixels,

https://doi.org/10.1017/S0022112010005604 Published online by Cambridge University Press

respectively. Five hundred image pairs were acquired for both the time-averaged and phase-averaged measurements. The cameras were mounted at a perpendicular distance of approximately 1 m to the laser light, such that the distance between pixels is $\sim$20 μm. The free-stream velocity (10 m s^{-1}) corresponds to an average displacement of approximately 8 pixels, with an approximate error of 0.1 pixels, which corresponds to a maximum error of $\pm$1.25 % of the free-stream velocity ($\pm$0.125 m s^{-1}).

Data on multiple spanwise planes (1 mm apart, see figure 2) were acquired along the central region of the span (i.e. the centre jet in figure 2*b*). Note that the solid lines in figure 2(*c*) represent the planes where data were acquired, while the dashed lines are the symmetry planes (25 planes). Stereoscopic PIV data collected on these planes were within a window size of about 25 mm $\times$ 25 mm. The data from all the planes were then reconstructed into a volume to provide the 3-D interaction domain between the synthetic jet and the crossflow.

The strength of the synthetic jets (relative to the free-stream velocity) for an incompressible flow is quantified using the momentum coefficient per jet $C_{\mu c}$, defined as

$$C_{\mu c} = \frac{U_j^2 h}{\frac{1}{2} U_\infty^2 c}, \tag{2.1}$$

where U_∞ is the free-stream velocity, c is the wing chord, h is the width of the synthetic jet orifice, and U_j is the time-averaged jet velocity at the exit of the slot during the outstroke defined as

$$U_j = \frac{1}{T} \int_0^{T/2} u_j(t)\, \mathrm{d}t, \tag{2.2}$$

where T is the time period of the synthetic jet cycle, and $u_j(t)$ is the velocity at the centre of the jet exit (measured using a hot-wire sensor in the experiments without a crossflow). Note that the spanwise distribution of the velocity was uniform over 90 % of the jet span. Another parameter used to quantify the relative strength of the synthetic jet is the blowing ratio C_b, defined as

$$C_b = \frac{U_j}{U_\infty}. \tag{2.3}$$

In the experiments, six actuation levels were selected (in addition to the baseline case), where the momentum coefficient ranged from 3.96×10^{-4} to 1.42×10^{-2} (corresponding to a range of blowing ratios from 0.2 to 1.2 with an increment of 0.2). These actuation cases are labelled from $C_{\mu c1}$ to $C_{\mu c6}$. Furthermore, a frequency of 2500 Hz (which is not the resonance frequency of the piezoelectric disk) was selected as the driving frequency for the jets (where all the jets produced the same velocity and all operated in-phase). Note that the characteristic frequency of the flow over the aerofoil (based on the 'time of flight') is about 66 Hz, and thus the actuation frequency is more than an order of magnitude higher, which, as shown later, results in a virtual aero-shaping of the wing.

3. Numerical set-up and methodology

In addition to the experiments, 3-D flow computations were carried out for a single finite-span synthetic jet flush-mounted on the surface of a unit wing section. The numerical set-up matched not only the physical parameters (e.g. free-stream and blowing ratio) but also the physical dimensions (e.g. width and aspect ratio of the jet slit, orientation and location of jet, and flow control cavity including slot

https://doi.org/10.1017/S0022112010005604 Published online by Cambridge University Press

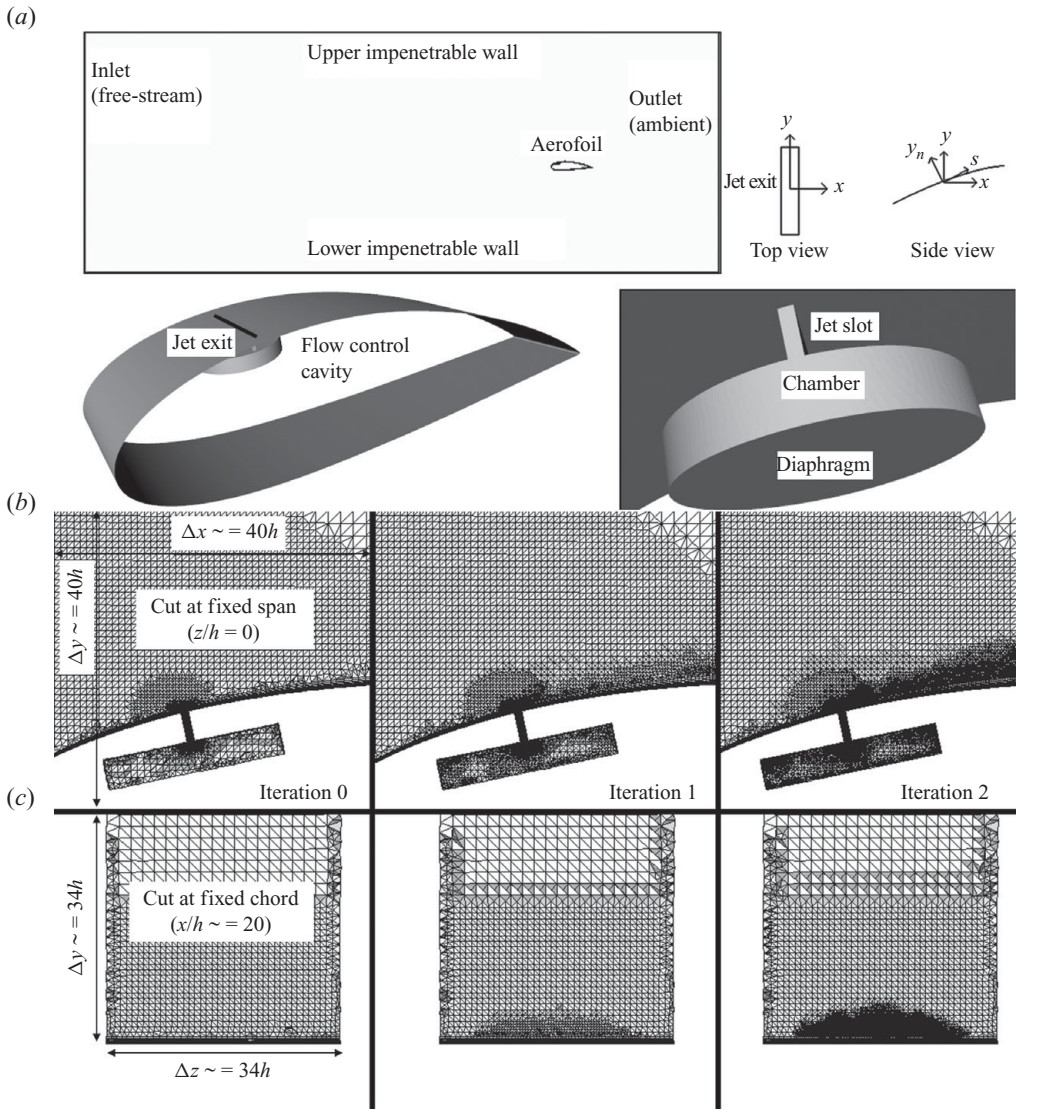


FIGURE 3. Computational configuration including boundary conditions and geometric details of the finite-span synthetic jet (*a*) along with spanwise (*b*) and chordwise (*c*) cuts of meshes. The left column of mesh cuts is the initial mesh while the middle and right columns are of the first and second mesh adaptation iterations.

and chamber). Numerical simulations of two actuated cases were performed, one corresponding to $C_{\mu c} = 1.58 \times 10^{-3}$ or $C_b = 0.4$ (i.e. in the lower range where non-negligible effects due to jets were observed experimentally), and another corresponding to $C_{\mu c} = 1.42 \times 10^{-2}$ or $C_b = 1.2$ (i.e. the highest actuation level). These cases are referred to as $C_{\mu c2}$ and $C_{\mu c6}$, respectively.

The computational configuration, including boundary conditions and geometric details, is shown in figure 3, where the flow control cavity includes the slot and chamber with the diaphragm surface at the opposite end (matching the experimental set-up). The boundary conditions were applied as follows: (i) free-stream velocity was prescribed at the tunnel inlet, (ii) upper and lower tunnel walls (about four

https://doi.org/10.1017/S0022112010005604 Published online by Cambridge University Press

chord lengths from the aerofoil) were considered as impenetrable or slip walls, (iii) symmetry boundary conditions were used at the side surfaces (not shown in the figure), (iv) aerofoil and cavity surfaces (except diaphragm) were considered as no-slip walls, (v) at the circular diaphragm, a velocity profile was applied to match the disk motion and (vi) ambient pressure was prescribed as a natural boundary condition at the tunnel outlet. Note that the displacement of the actuator diaphragm was not modelled in the simulations; instead, a parabolic velocity profile (along the radius of the diaphragm) with a sinusoidal variation in time was prescribed such that both the amplitude (for each momentum coefficient) and frequency (fixed at 2500 Hz) matched the experiments. The velocity amplitude was determined based on the hot-wire data collected at the centre of the jet exit without a crossflow. It is worth mentioning that consideration of the slot and chamber of the jet cavity, along with a sinusoidal actuation in time via a prescribed velocity profile, has been shown to essentially model and match the experimental conditions (e.g. Muppidi & Mahesh 2005; Kotapati *et al.* 2007). Also, note that in the simulations only a single synthetic jet in the span was considered, as it was determined experimentally (see figure 4) that the flow is quasi-periodic along the mid-span section of the wing.

The numerical simulations solved the incompressible Navier–Stokes equations. Spatial discretization was carried out with a stabilized finite-element method (i.e. the streamline/upwind Petrov–Galerkin (SUPG) method; see Whiting & Jansen 2001), while temporally implicit integration was performed based on a generalized-alpha method (see Jansen, Whiting & Hulbert 2000). The resulting nonlinear algebraic equations were linearized to yield a system of equations, which were solved using iterative procedures, e.g. generalized minimal residual method (GMRES) (Saad & Schultz 1986). Furthermore, mesh resolution was increased in an adaptive fashion, since for problems of practical interest, increasing the mesh resolution to a level necessary for acceptable accuracy in a globally uniform fashion would introduce prohibitive demands on the computational resources. In adaptive mesh methods, mesh resolution and configuration are determined and modified in a local fashion based on the spatial distribution of the numerical solution and approximation errors associated with it (for details see Sahni *et al.* 2006).

In this study, we have employed boundary-layer mesh adaptivity (Sahni *et al.* 2008) that maintains favourable attributes of such meshes, i.e. high-aspect-ratio, orthogonal, layered and graded elements near the viscous walls. Figure 3(*b,c*) shows the resulting adapted meshes, where the mesh in the left column is an initial mesh and those in the middle and right columns are subsequently adapted meshes. Note that each mesh adaptation step is based on the numerical solution computed in a simulation cycle on the current mesh, which we refer to as one-mesh adaptation iteration. In each actuated case, four mesh adaptation iterations were carried out (the first two iterations are shown in figure 3), which resulted in an adequate mesh with about 11.5–15 million nodes and 65–80 million elements. Implicit time integration was performed with 360 time steps of constant size in each jet cycle (computations with 180 time steps in a cycle showed no significant differences).

The resolution used in the current numerical simulations was adequate to resolve the physical scales well into the dissipation range in the vicinity of the jet based on the energy spectra (see figure 19), i.e. within the interrogation domain of interest, the mesh resolution was appropriate for DNS, while far outside the interrogation domain, the mesh resolution was smoothly coarsened to that corresponding to LES (e.g. see Bazilevs *et al.* 2007; Trofimova *et al.* 2009). Specifically, mesh spacing used in the vicinity of the jet was about 2 Kolmogorov length-scale units. The Kolmogorov length

https://doi.org/10.1017/S0022112010005604 Published online by Cambridge University Press

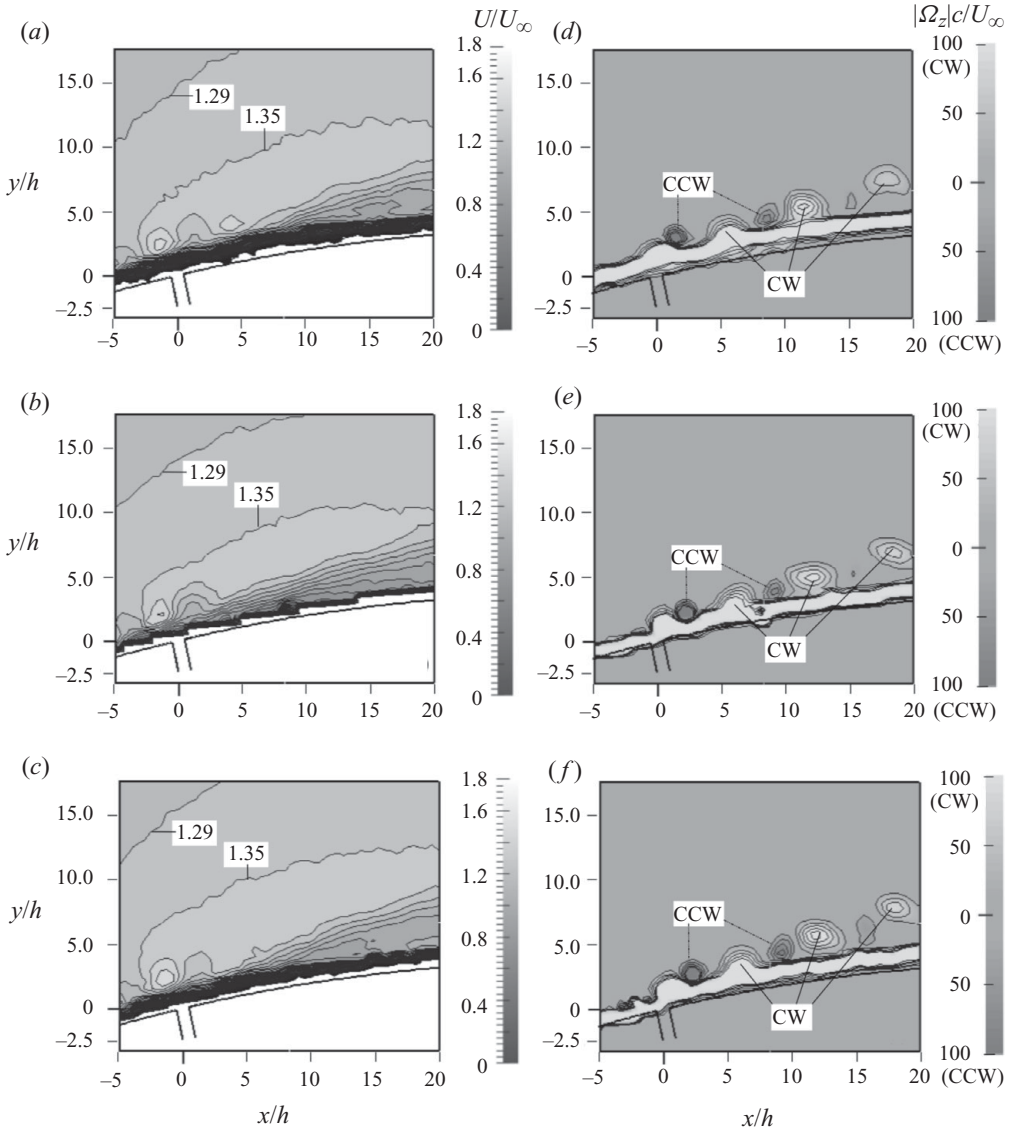


FIGURE 4. Experimental data of the time-averaged total velocity (*a–c*) and phase-averaged spanwise vorticity (*d–f*) fields across the centreplane of jets 2 (*a*, *d*), 3 (*b*, *e*) and 4 (*c*, *f*). In phase-averaged vorticity plots the background colour value is at zero, implying that a lighter shade (than the background colour) indicates the CW vorticity whereas a darker shade shows the CCW vorticity.

scale was estimated to be 20 μm downstream of the jet based on an analysis of a time trace of velocity data and a one-dimensional surrogate for the dissipation rate (e.g. see Pope 2000; Mallinson *et al.* 2004). In terms of viscous length scales or wall units, the wall-normal spacing for the first point off the wall was within 1 unit, while the streamwise and spanwise spacing was about 5 units.

Average quantities, including phase-locked averages, were computed based on samples collected for about 50 cycles in the low-momentum coefficient case, whereas for the high-momentum coefficient case samples over 350 (or above) cycles were used.

https://doi.org/10.1017/S0022112010005604 Published online by Cambridge University Press

To be able to perform these large-scale flow computations in a reasonable time frame, parallel computers were used. Note that the current flow solver scales strongly to $O(100\,000)$ processor cores (Sahni *et al.* 2009), allowing it to be a scalable tool for such practical cases. TeraGrid computer systems (Ranger at TACC and Kraken at NICS) were used to perform the numerical computations, where calculations for 50 jet cycles on the finest adapted mesh utilized about 15 h (in terms of wall-clock time) on 8192 processor cores. For post-processing and visualization, we used the computer system of Spur at TACC (another TeraGrid system).

4. Results

In this section, the near-field 3-D interactions between the finite-span synthetic jet and crossflow are discussed for different blowing ratios, and a detailed comparison between the experimental measurements and numerical results is presented. In order to isolate the effect of the blowing ratio and to limit the amount of experiments and numerical simulation, a single Reynolds number and an angle of attack were selected such that there is no separation in the vicinity of the synthetic jets. Section 4.1 provides validation of the assumption that the flow is spanwise periodic in the mid-span of the wing and thus only a spanwise section of the flow field can be considered. Section 4.2 presents the time-averaged flow field in the vicinity of the synthetic jet, while § 4.3 discusses the corresponding instantaneous and phase-averaged flow fields. Note that throughout the paper, momentum coefficient and blowing ratio are used interchangeably. This can only be valid for the incompressible flow and when the orifice and aerofoil dimensions are kept fixed, which is the case in the present work.

4.1. *Quasi-periodic flow along the mid-span: actuated cases*

To simplify both the experimental and numerical efforts, an assumption was made that the baseline flow field over a portion (mid-section) of the finite wing is two-dimensional and the actuated flow is quasi-periodic along the span. However, no assumption is made regarding the interaction domain (between the synthetic jet and the crossflow), which, as shown later, is highly three-dimensional. These assumptions were verified experimentally and are presented in figure 4. It is noteworthy that Greenblatt & Washburn (2008) showed experimentally that the flow over a finite-span wing with no sweep (with a similar aspect ratio as in the present model) is quasi-two-dimensional over a large portion of the span. To verify that the actuated flow field is quasi-periodic along the span (in the middle section), synthetic jets were activated at the highest blowing ratio of 1.2. The rationale is that if the flow field for the highest blowing ratio is periodic, then actuated cases with lower blowing ratios must be periodic as well. Figure 4 presents contour plots of the actuated flow field in the vicinity of the synthetic jets, where data were acquired across the centreplane of jets 2–4 (see notation in figure 2). The figure shows time-averaged total velocity fields (figure 4*a–c*) and phase-averaged spanwise vorticity fields (figure 4*d–f*; at a phase of $\phi = 240^\circ$ during the synthetic jet-driving cycle, where the start of the jet cycle ($\phi = 0^\circ$) is considered at the beginning of the blowing portion of the cycle. Note that the phase is measured with respect to the driving signal and not the velocity output of the slot, which is about 30° off. This phase difference suggests that compressibility effects are present (Gallas *et al.* 2003). In the present work, the numerical data were shifted by a 30° phase to match the experimental input. Furthermore, in the phase-averaged vorticity plots, the background colour value is set to zero, implying that lighter shades (than the background colour) indicate clockwise (CW) vorticity,

https://doi.org/10.1017/S0022112010005604 Published online by Cambridge University Press

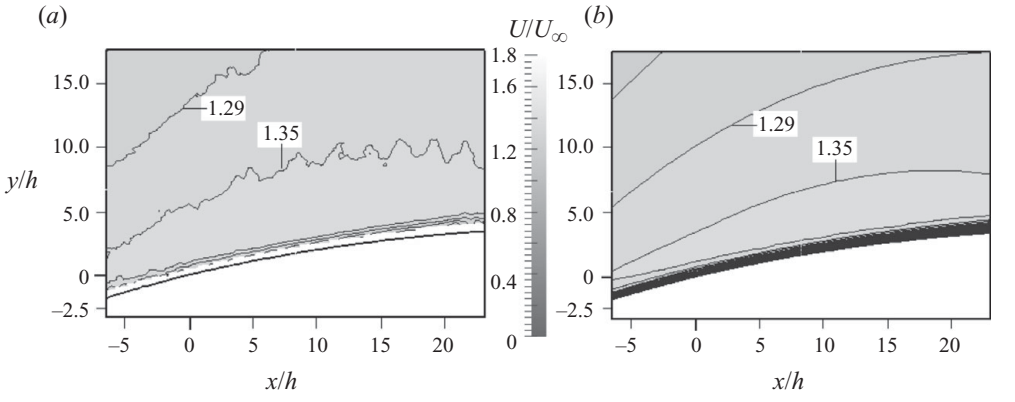


FIGURE 5. Contour plots of the total velocity across the centreplane of jet 3; experiment (*a*) and simulation (*b*). Baseline case.

whereas darker shades represent counterclockwise (CCW) vorticity. The velocity, as well as the vorticity, fields at the three planes show similar flow structures from three different jets in the mid-span, thus justifying the assumption made above. Therefore, the focus is placed on the centre jet (jet 3 in figure 2), and a detailed discussion on the velocity and vorticity fields, based on both experimental and numerical data, is presented in the following.

4.2. *Time-averaged flow field*

Figures 5 and 6 present comparisons of the time-averaged velocity field between the experimental measurements and numerical simulations for the baseline case. Contour plots of the total velocity across the centreplane of jet 3 are presented in figure 5; this interrogation domain, in the vicinity of the jet, is selected to enable a detailed study of flow structures and interactions due to actuation. A more quantitative comparison between the experimental and numerical results is obtained by showing line plots at different streamwise locations, as presented in figure 6. Note that the location of each line plot is presented at the top of figure 6 (where five streamwise locations are considered); the lines are normal to the surface and include downstream as well as upstream locations very near to the jet orifice. The distance normal to the surface (referred to as y_n) is normalized by h (the width of the synthetic jet orifice) for comparison with the forced cases that follow. Velocity profiles on subsequent lines are offset by a unit distance of $U/U_\infty = 1$. Note that the experimental data (symbols) are plotted from a distance h away from the surface (i.e. from $y_n/h = 1.0$) due to the limitations of the PIV measurements very near to a solid curved surface (i.e. within 0.75 mm).

Next, the time-averaged interaction between the synthetic jet and crossflow is presented in figures 7, 8 and 10, using the same interrogation domain as the baseline case, where the experimental measurements are compared with the numerical results. Two actuated cases are examined here: $C_{\mu c2}$ and $C_{\mu c6}$ (corresponding to blowing ratios of $C_b = 0.4$ and $C_b = 1.2$, respectively). Figure 7 presents contour plots of the total velocity across the centreplane of jet 3, where the experimental results are shown in figures 7(*a*) and 7(*b*), while the numerical results are displayed in figures 7(*c*) and 7(*d*). The forcing levels corresponding to $C_b = 0.4$ and $C_b = 1.2$ are presented in figures 7(*a*, *c*) and 7(*b*, *d*), respectively. The introduction of the synthetic jet into the crossflow yields three primary effects on the mean flow (compared with the baseline flow field):

https://doi.org/10.1017/S0022112010005604 Published online by Cambridge University Press

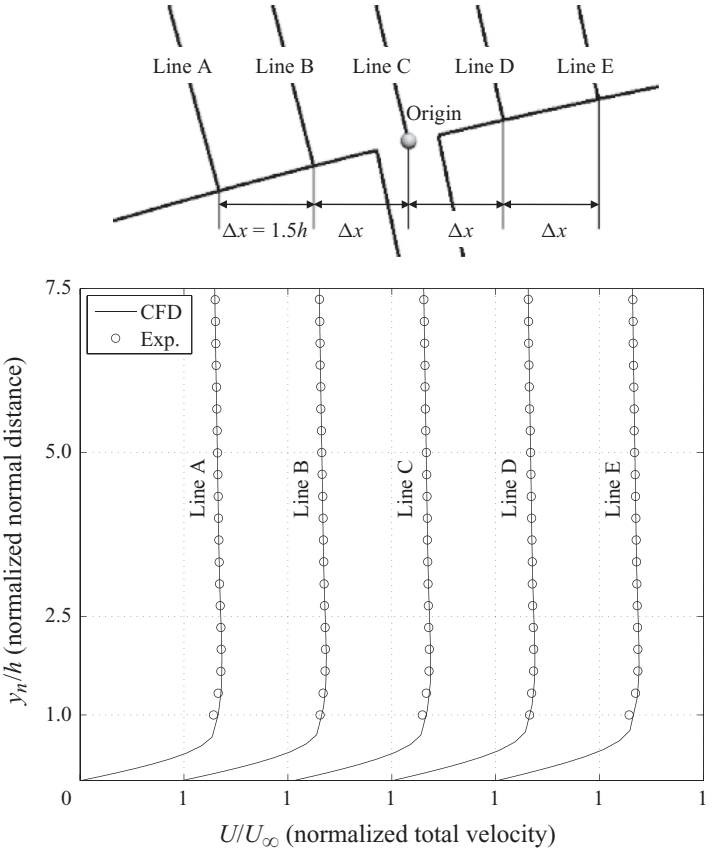


FIGURE 6. Time-averaged total velocity profiles along five lines normal to the surface at $x/h = -3$ (line A), -1.5 (line B), 0 (line C at jet exit), 1.5 (line D) and 3 (line E). Velocity profiles on subsequent lines are offset by a unit distance of $U/U_\infty = 1$; experiment (symbols) and simulation (lines). Baseline case.

(i) reduced velocity just upstream of the jet, (ii) higher velocity downstream of the jet and (iii) thickening of the boundary layer downstream of the jet. These effects are much more pronounced for the case with a higher blowing ratio. Furthermore, as can be seen in figure 7, the numerical results capture the features of the measured flow interactions.

The effect of the synthetic jet on the velocity field was also examined using line plots at the same locations as in the baseline case (discussed in figure 6). Figure 8 shows the total velocity profiles along the same five lines used in figure 6, for $C_b = 0.4$ (figure 8*a*) and $C_b = 1.2$ (figure 8*b*). The velocity profiles on subsequent lines are offset by a unit distance of $U/U_\infty = 1$. The plots include the experimental measurements (symbols) and simulation results (lines). These plots show that as the blowing ratio increases, the effect of the synthetic jet is felt farther away from the wall and a velocity maximum in the velocity profile is obtained downstream of the jet. Though these effects are present in the experimental and numerical data, the increase in the near-wall velocity is more strongly predicted in the simulations than observed in the experiments (especially in the high blowing ratio case). In a measurement window with such a strong velocity gradient, uncertainty in PIV increases significantly, specifically for the maximum jet

https://doi.org/10.1017/S0022112010005604 Published online by Cambridge University Press

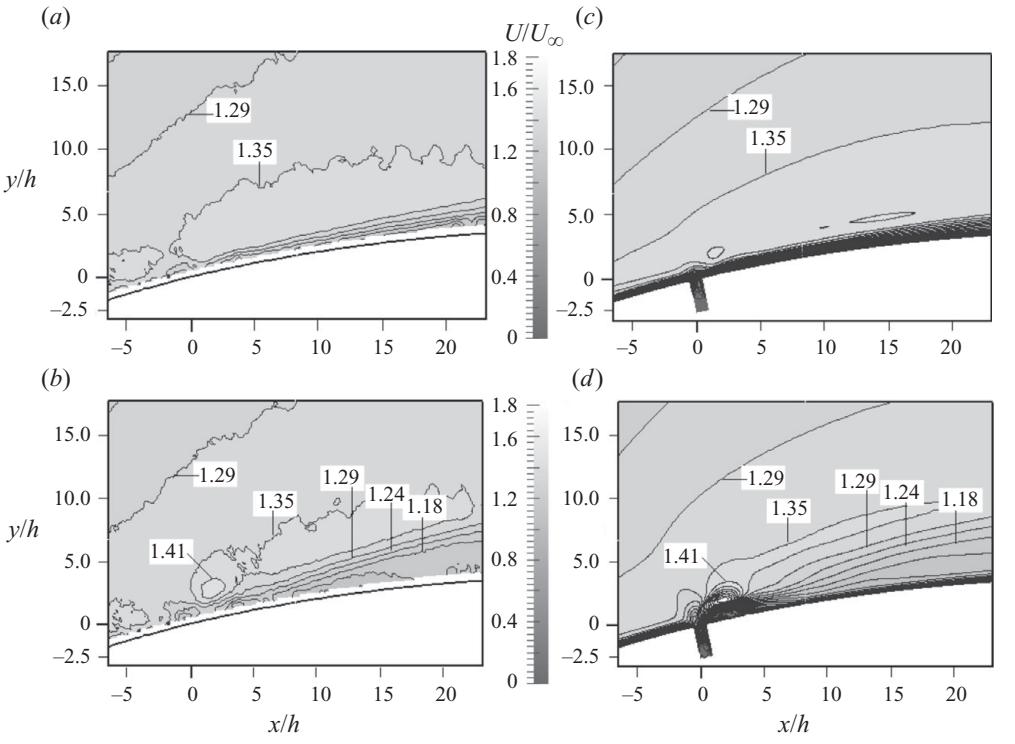


FIGURE 7. Contour plots of the total velocity across the centreplane of jet 3; experiments (a, b) and simulations (c, d). Forced cases with $C_b = 0.4$ (a, c) and 1.2 (b, d).

speed (see Yao *et al.* 2004). Similar trends have also been observed in other synthetic jet validation studies comparing experimental and numerical results, for example, in velocity profiles at a downstream distance of two orifice diameters in the case of a circular synthetic jet mounted on a flat plate in Rumsey (2004).

Because of the finite span of the synthetic jet, the interaction between the jet and crossflow is expected to be three-dimensional. Therefore, time-averaged iso-total velocity surfaces, based on the volumetric data over a spanwise strip of $z/h = 32$, were calculated and are presented in figure 9. The spanwise extent of this interrogation domain was selected such that it is centred at the mid-span of jet 3 and extends $L_z/4$ (quarter span of the jet slit) from the edge of the slit on each side (see figure 2). Furthermore, in figure 9 the effects of the blowing ratio on the flow interaction and the formation of the secondary flow structures were also explored. Six levels of blowing ratios, i.e. $C_b = 0.2$, 0.4, 0.6, 0.8, 1.0 and 1.2, which were considered experimentally, are shown in figure 9$(a–f)$, respectively, where an iso-total velocity surface is shown at a level of $U/U_\infty = 1.3$. For all blowing ratios, the interaction domain consists of secondary flow structures. Furthermore, as C_b increases, the interaction domain is affected as follows: (i) the penetration of the jet into the crossflow is increased, (ii) three-dimensionalities begin to appear closer to the slit, (iii) the spanwise wavelength of the secondary structures in the mean flow increases and (iv) the spanwise extent of the interaction domain decreases. The trends in (i) and (ii) are expected, as the jet becomes stronger in the crossflow, where mid-range cases (with $C_b = 0.6$ and $C_b = 0.8$) exhibit combined features from the low blowing ratio range (with $C_b = 0.2$ and $C_b = 0.4$) as well as from the high blowing ratio range (with $C_b = 1.0$ and

https://doi.org/10.1017/S0022112010005604 Published online by Cambridge University Press

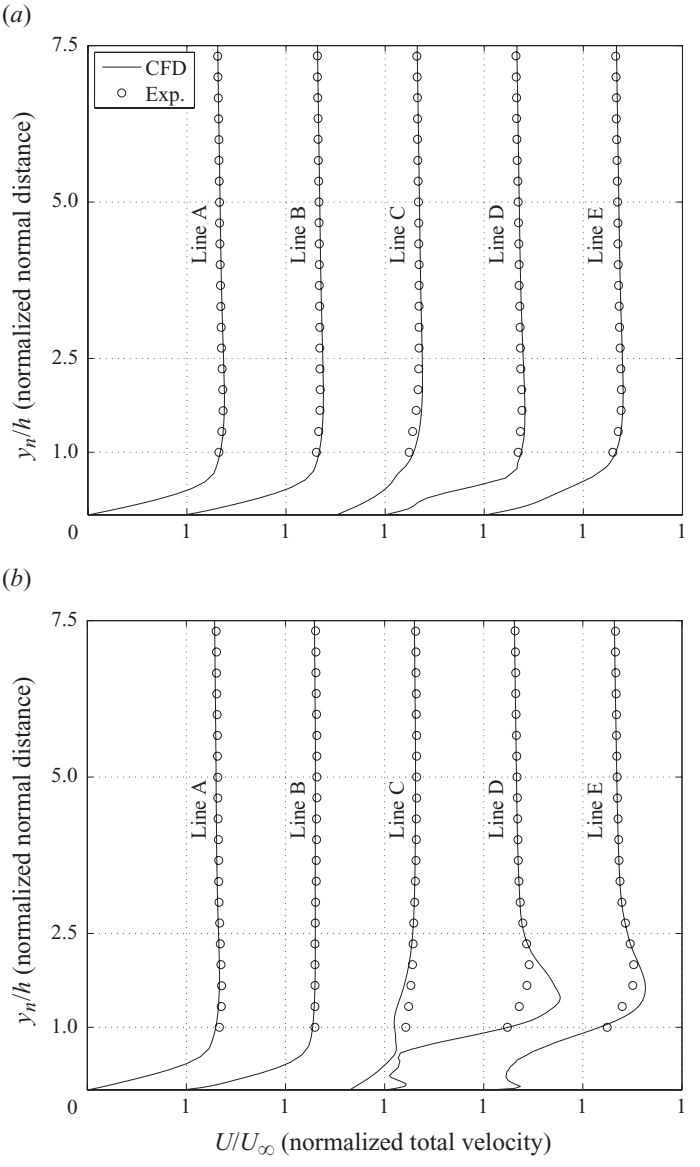


FIGURE 8. Time-averaged total velocity profiles along five lines normal to the surface at $x/h = -3$ (line A), -1.5 (line B), 0 (line C at jet exit), 1.5 (line D) and 3 (line E). Forced cases with $C_b = 0.4$ (*a*) and 1.2 (*b*). Velocity profiles on subsequent lines are offset by a unit distance of $U/U_\infty = 1$; experiments (symbols) and simulations (lines).

$C_b = 1.2$), namely in the mid-blowing ratio range, flow structures are two-dimensional very near the slit, similar to the low range, but they merge and lift off at downstream locations, similar to the high range. On the other hand, it is noteworthy that the trends in (iii) and (iv) are similar to those shown by Amitay & Cannelle (2006) for a finite-span synthetic jet issued into a quiescent flow (in their work, the strength of the synthetic jet was determined using the stroke length, L_0, due to the absence of a free stream). Moreover, Amitay & Cannelle (2006) showed that the strength of the

https://doi.org/10.1017/S0022112010005604 Published online by Cambridge University Press

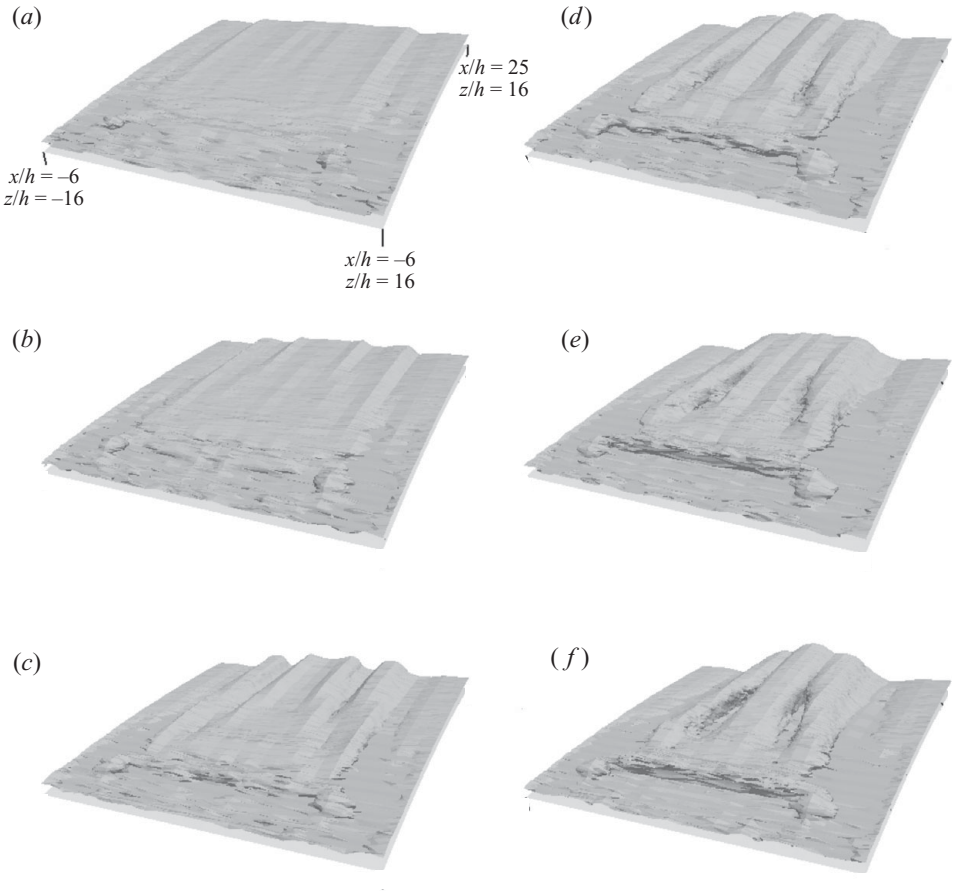


FIGURE 9. Effect of the momentum coefficient on the time-averaged (volumetric) flow field. Experimental data for six actuated cases: $C_b = 0.2$ (*a*), 0.4 (*b*), 0.6 (*c*), 0.8 (*d*), 1.0 (*e*) and 1.2 (*f*). Iso-surface of total velocity at $U/U_\infty = 1.3$. In (*b–f*), x/h and z/h values are the same as in (*a*).

secondary flow structures and their spanwise wavelength also vary with the aspect ratio of the synthetic jet slit.

Two actuated cases that were also considered numerically are compared with experimental results in figure 10. The experimental results are shown in figures 10(*a*) and 10(*b*) while the predictions from simulations are presented in figures 10(*c*) and 10(*d*) for $C_b = 0.4$ and $C_b = 1.2$ (figures 10*a*, *c* and 10*b*, *d*, respectively). As before, one can note that the interaction of the synthetic jet with the crossflow results in a blockage of the main flow just upstream of the slit, whereas downstream of the slit it exhibits well-organized streamwise (or secondary) structures in the mean flow. Furthermore, in the $C_b = 0.4$ case, multiple small and organized streamwise-oriented secondary structures are formed in the mean flow, which is clearly evident from the numerical data. However, due to the limited spatial resolution of PIV measurements, these small structures are not well captured in the experimental data. This small-amplitude waviness in the distribution corresponds to the development of secondary streamwise vortical structures, as will be discussed later in detail using figures 11 and 12. These secondary flow structures are organized in a symmetric fashion about the

https://doi.org/10.1017/S0022112010005604 Published online by Cambridge University Press

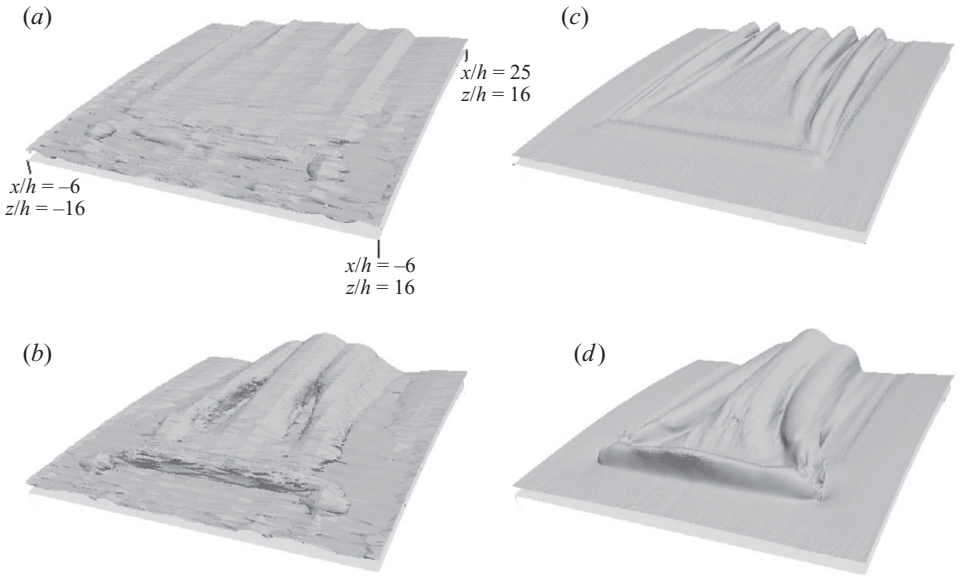


FIGURE 10. Time-averaged iso-total velocity surface at a level of $U/U_\infty = 1.3$ (note that no relative scale factor is applied between different coordinates). Experiments (a, b) and simulations (c, d) for forced cases with $C_b = 0.4$ (a, c) and 1.2 (b, d). In $(b–d)$, x/h and z/h values are the same as in (a).

centreplane of the jet. In the high blowing ratio case, with $C_b = 1.2$ these structures are much larger both in the wall-normal and spanwise (larger wavelength) directions. Furthermore, they appear to be merged together, namely with a lobe in the middle and a lobe near each end (also note that these structures develop immediately downstream of the slit, unlike the low blowing ratio case). It is noteworthy that these secondary flow structures are formed due to the finite span of the synthetic jet and can play an important role in various flow control applications (e.g. separation control and virtual aero-shaping).

To gain a better understanding of the spatial evolution of these flow structures, the high-resolution numerical data are presented over cross-stream planes at four different chord locations, including one at the jet slit and three downstream of the slit, i.e. at $x/h = 0$ (at the jet exit), $x/h = 5$, $x/h = 10$ and $x/h = 15$; all planes are in the wall-normal direction and only half of the span is presented (due to symmetry). Two actuated cases with $C_b = 0.4$ and $C_b = 1.2$ are examined in figures 11 and 12, respectively. At each plane, velocity and pressure fields are presented. In the velocity field, vectors are based on cross-stream (or in-plane) components whereas the background colour is based on the streamwise component. The pressure field is non-dimensionalized in the form of pressure coefficient based on the free-stream as $C_p = (p - p_\infty)/q_\infty$ (where $q_\infty = 1/2\rho_\infty U_\infty^2$ is the dynamic pressure at the free-stream).

Figure 11 shows the evolution of the spanwise structures for the low blowing ratio case. At the orifice plane (figure 11*a*), a counterclockwise discrete vortex can be seen in the velocity vector field at the edge of the slit (located at $z/h = 10.67$). At this spanwise location, near the edge of the slit, a region of low pressure exists, as is evident from the pressure field. Immediately above the slit, a relatively low pressure exists up to a normal distance of about half a slit width $(h/2)$ and above that a high pressure is built up. This is due to the fact that the jet causes a blockage to the

https://doi.org/10.1017/S0022112010005604 Published online by Cambridge University Press

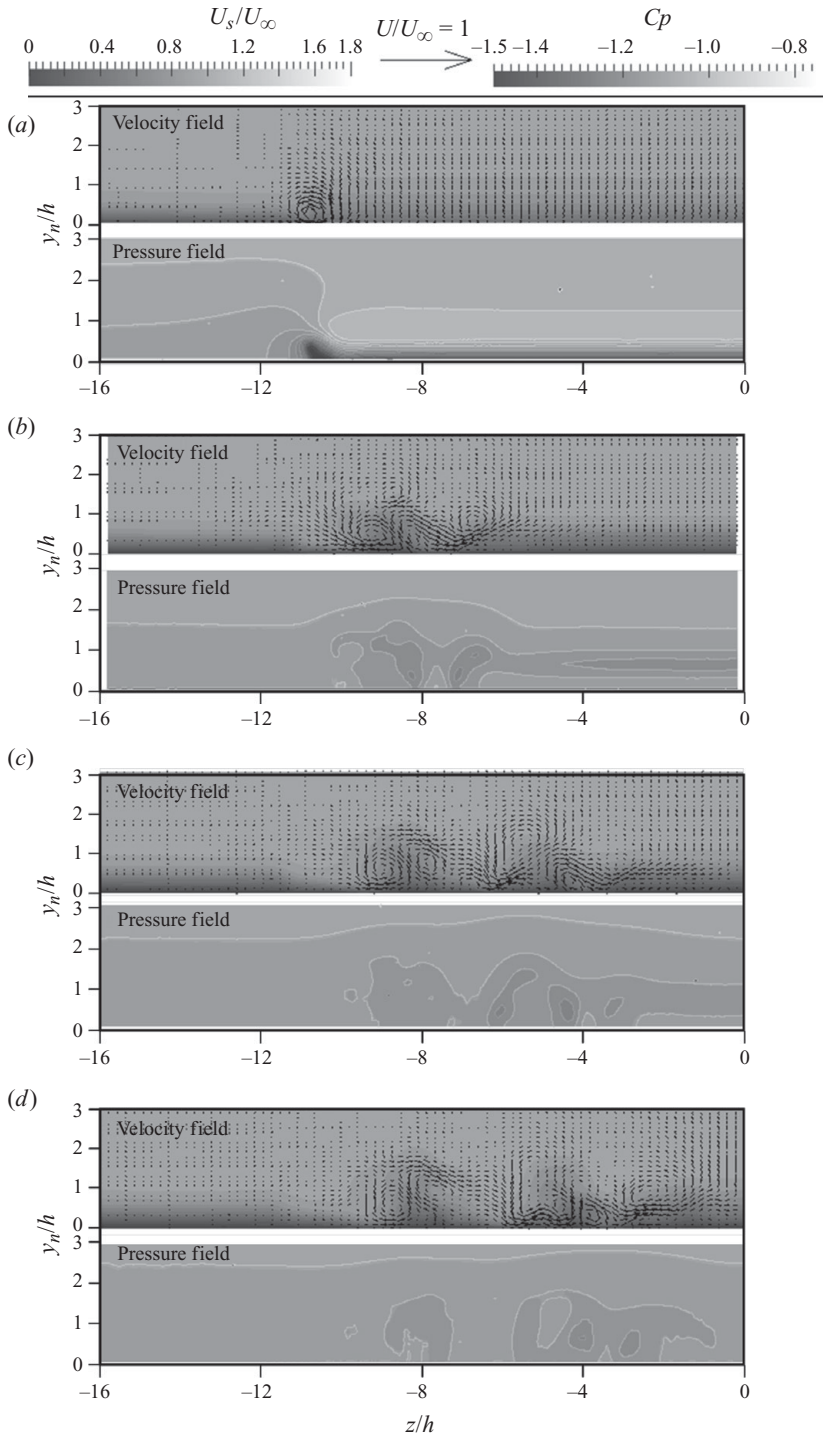


FIGURE 11. Time-averaged velocity and pressure fields based on numerical data for an actuated case with $C_b = 0.4$. Four planes normal to the surface, covering half-span (due to symmetry), are considered at $x/h = 0$ (at jet exit) (*a*), 5 (*b*), 10 (*c*) and 15 (*d*). Velocity vectors are based on cross-stream (or in-plane) components, whereas the background is based on the streamwise component.

https://doi.org/10.1017/S0022112010005604 Published online by Cambridge University Press

crossflow, as mentioned in figures 9 and 10. It is noteworthy that a higher upstream pressure in the mean flow is also observed in the case of a steady jet in a crossflow (e.g. Muppidi & Mahesh 2005). Moreover, the mean flow in this plane is two-dimensional for about 95 % of the slit's span, except at the edge.

The streamwise vortex formed at the edge of the slit perturbs the 2-D flow as it is advected downstream and moves inwards (as can be seen in the second cross-stream plane in figure 11*b*), where the flow is two-dimensional for about 60 % of the slit's mid-span. These interactions lead to the development of cross-stream velocity components, altering the streamwise component (see background colour in the velocity plots) and forming counter-rotating vortical structures along the span. Farther downstream, multiple distinct secondary streamwise structures are formed along the entire span of the slit, leading to a highly 3-D interaction, as is evident in the third and fourth planes in figures 11(*c*) and 11(*d*), respectively. These multiple secondary structures are responsible for the streak-like pattern or small waviness observed in the mean flow for the low blowing ratio case (i.e. in the iso-total velocity surface in figure 10*a*, *c*).

Similarly, figure 12 presents the spanwise structures for the high blowing ratio case. As expected, a much larger streamwise vortex exists at the edge of the slit (figure 12*a*), as compared to the low blowing ratio (figure 11*a*). For the high blowing ratio case, the region with low pressure is also larger both at the edge of the slit and immediately above the slit, indicating that the extent of the jet and crossflow interaction is increased due to a stronger jet. As in the low blowing ratio case, the mean flow in this case is two-dimensional in the cross-stream plane at the orifice but only for about mid-85 % of the slit's span. At this level of actuation, secondary structures are formed closer to the synthetic jet orifice, as is evident in the second cross-stream plane. In this plane, significant cross-stream components and counter-rotating vortical structures are developed, where the spanwise component dominates and 3-D interactions exist in almost the entire span of the slit (unlike the low blowing ratio case). This is in accord with the iso-total velocity plot shown in figures 10(*b*) and 10(*d*), where three-dimensionalities can be seen just downstream of the slit. The pressure field in the second plane further supports this observation, where a low-pressure region exists in the centre of these lobe-like structures. It is also clear that the normal-to-the-surface extent of these structures is larger, as compared with the low blowing ratio case. Farther downstream (i.e. third and fourth planes in figures 12*c* and 12*d*, respectively), these secondary structures appear to merge together, unlike the low blowing ratio case, which exhibits multiple distinct structures. Also, note that the farther downstream planes, for the high blowing ratio case, show, as before, that the spanwise extent of these structures and interactions is reduced. The reason for such flow structures and interactions will become clearer with the help of instantaneous and phase-averaged flow fields, presented in the next subsection.

4.3. *Instantaneous and phase-averaged flow field*

In order to fully understand the formation and evolution of the secondary flow structures, one needs to examine the instantaneous and the phase-locked flow fields. Therefore, figures 13–17 present phase-averaged spanwise vorticity based on experimental and numerical results, while figures 18 and 20 present instantaneous spanwise vorticity, and figure 19 presents the energy spectra, based on numerical results. The terms clockwise (CW) and counterclockwise (CCW) are used to define the direction of the spanwise vorticity. Note that vorticity due to the crossflow boundary layer is in the clockwise direction.

https://doi.org/10.1017/S0022112010005604 Published online by Cambridge University Press

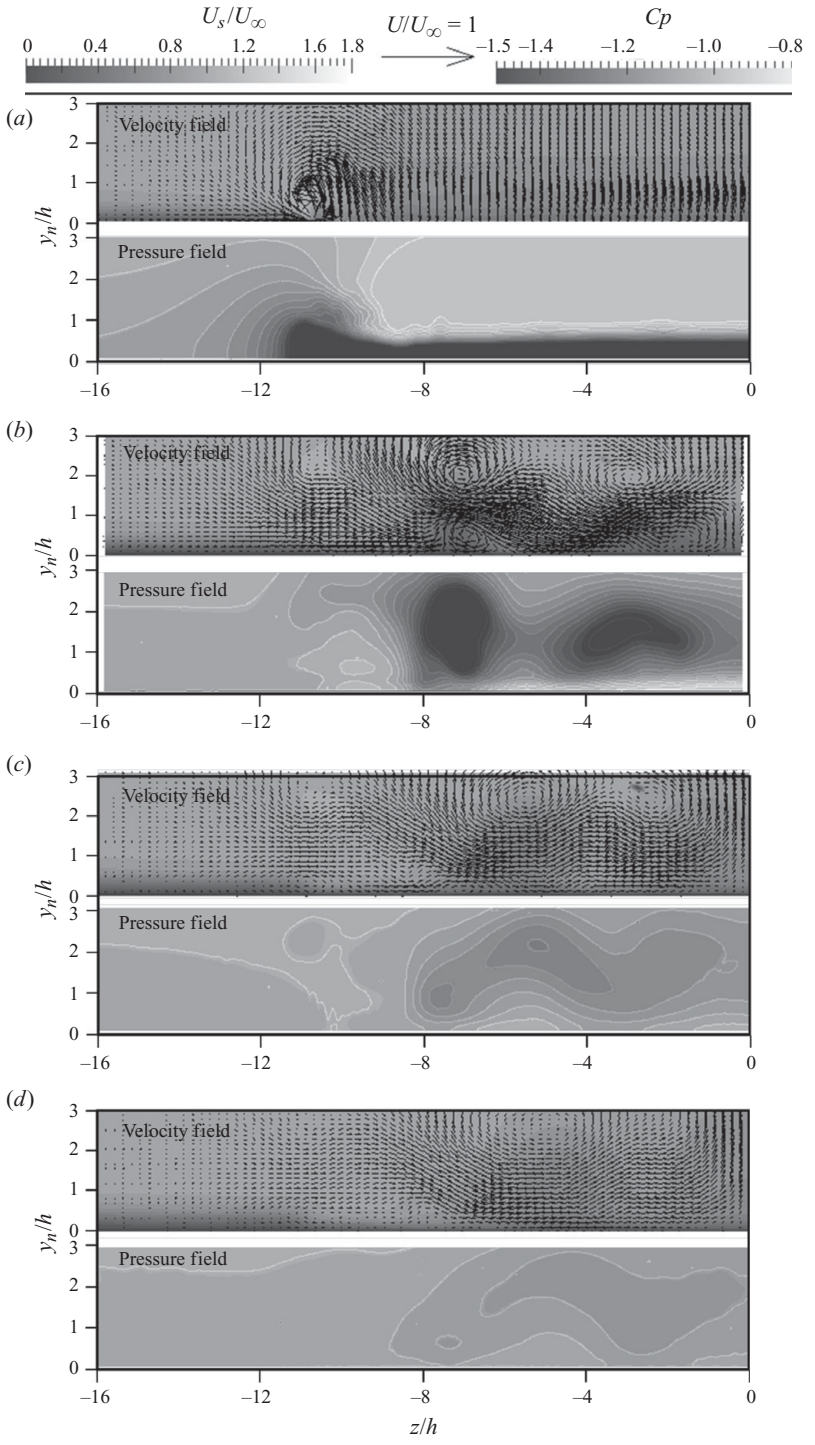


FIGURE 12. Time-averaged velocity and pressure fields based on numerical data for an actuated case with $C_b = 1.2$. Four planes normal to the surface, covering half-span (due to symmetry), are considered at $x/h = 0$ (at jet exit) (*a*), 5 (*b*), 10 (*c*) and 15 (*d*). Velocity vectors are based on cross-stream (or in-plane) components, whereas the background is based on the streamwise component.

https://doi.org/10.1017/S0022112010005604 Published online by Cambridge University Press

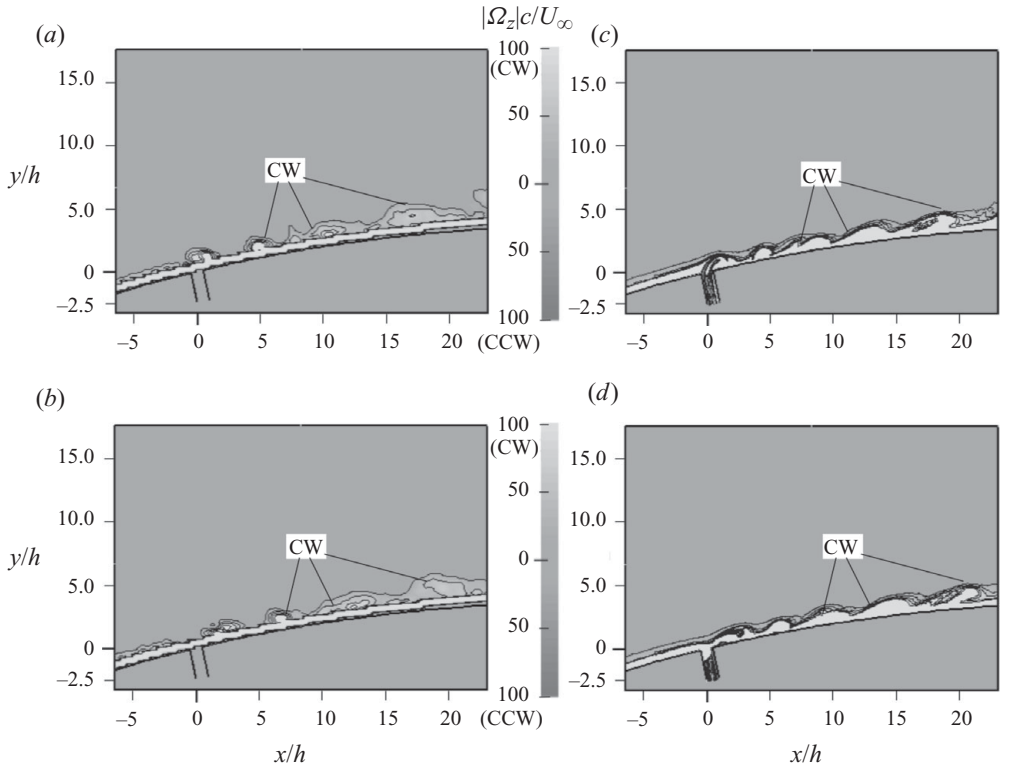


FIGURE 13. Centreplane comparison of the phase-averaged spanwise vorticity between experiments (a, b) and simulations (c, d) for an actuated case with $C_b = 0.4$ at two phases, $\phi = 120^\circ$ (a, c) and 240° (b, d). The lighter shade has been used for the CW vorticity and the darker shade for the CCW vorticity.

Figures 13–16 compare the experimental and numerical results of the phase-averaged spanwise vorticity. Figures 13 and 14 present data at the centreplane for two actuated cases with $C_b = 0.4$ and $C_b = 1.2$, respectively, whereas figures 15 and 16 provide a volumetric view of the same two actuated cases in terms of iso-vorticity surfaces. These figures include two phases of $\phi = 120^\circ$ and $\phi = 240^\circ$ in the synthetic jet cycle.

Figure 13 presents the actuated case with $C_b = 0.4$, where figures 13(a) and 13(b) show the experimental data, while figures 13(c) and 13(d) present the numerical data. The evolution of periodic vortical structures issued by the synthetic jet can be clearly seen in this interrogation window for both experimental and numerical results. Note that the CCW vorticity (associated with the synthetic jet) is absent in this case (outside the jet slot), as it is not strong enough to overcome the CW vorticity of the crossflow boundary layer. However, the periodic nature of the synthetic jet leads to a train of coherent (clockwise) vortices in the boundary layer that advects downstream with the main flow. Each vortex undulation corresponds to actuation caused in a synthetic jet cycle. At a phase of 120°, the vortical structure formed in the current jet cycle exists very close to the orifice (figures 13a and 13c), whereas by the phase of 240° it is advected downstream, as shown in figures 13(b) and 13(d). Furthermore, since here $C_b = 0.4$ (i.e. a weak jet), the vortical flow structures stay close to the surface.

https://doi.org/10.1017/S0022112010005604 Published online by Cambridge University Press

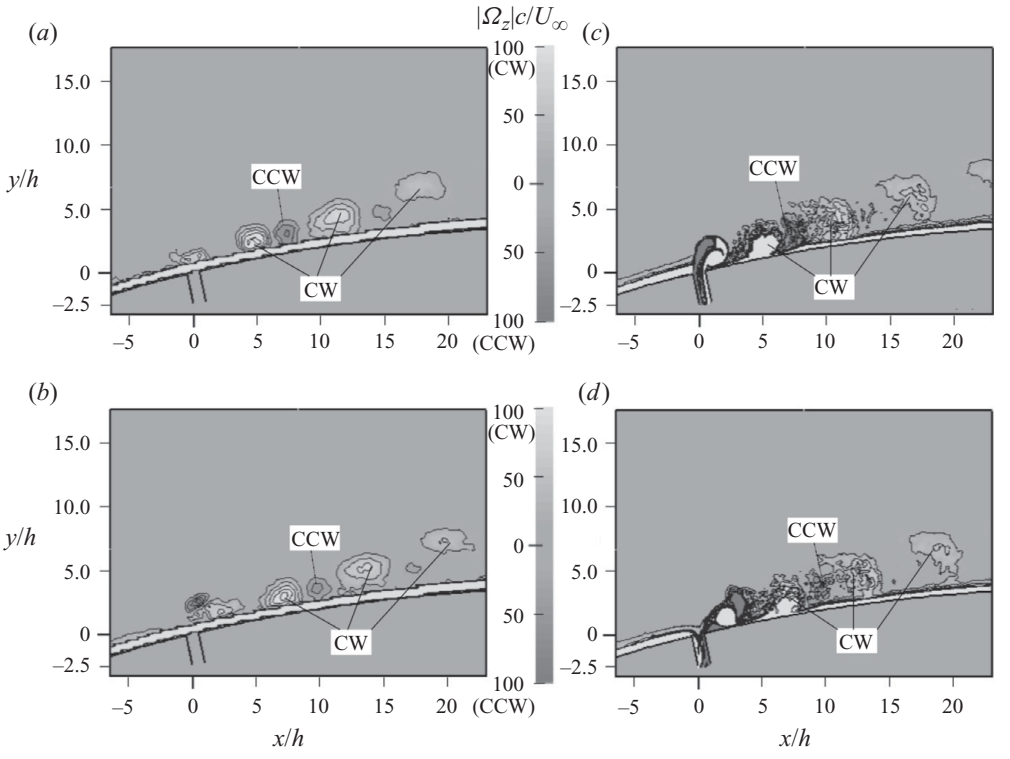


FIGURE 14. Centreplane comparison of the phase-averaged spanwise vorticity between experiments (a, b) and simulations (c, d) for an actuated case with $C_b = 1.2$ at two phases, $\phi = 120°$ (a, c) and $240°$ (b, d). Shades are the same as in figure 13.

Figure 14 shows phase-averaged spanwise vorticity for the case in which the synthetic jet is activated at a higher blowing ratio of $C_b = 1.2$. In this case, in contrast to the low blowing ratio case, both CW and CCW vortices are present and, furthermore, vortical structures are distinctly bigger than the lower blowing ratio case and penetrate much deeper into the main flow and eventually lift off the surface. Note, though, that the coherent structures based on phase-averaged numerical data appear to have limited statistical convergence, especially towards the end of the interrogation domain; this is because high levels of random motions exist in the high blowing ratio case, as will be shown later (in the instantaneous flow field). It is noteworthy that the phase-averaged fields collected in simulations are based on samples over 350 jet cycles for the high blowing ratio case, which are able to capture these coherent vortical structures but consume a substantial amount of computing resources (more samples will make these coherent structures more pronounced but at a significant cost). Nevertheless, numerical data are able to provide more details of the flow structures, especially around the orifice and also near to the solid curved surface of the aerofoil (where PIV measurements have limitations). These observations emphasize the complementary nature of experiments and simulations; what is relatively very hard for one technique is relatively easy for the other. At the phase of 120° (figures 14*a* and 14*c*), vortical structure issued from the jet orifice in the current cycle can be clearly seen just downstream of the jet slit. However, in contrast to the low blowing ratio case, a discrete counter-rotating vortex pair exists and is tilted due to the crossflow. At a later phase of 240° (figures 14*b* and 14*d*), the CCW vortex appears to roll over the

https://doi.org/10.1017/S0022112010005604 Published online by Cambridge University Press

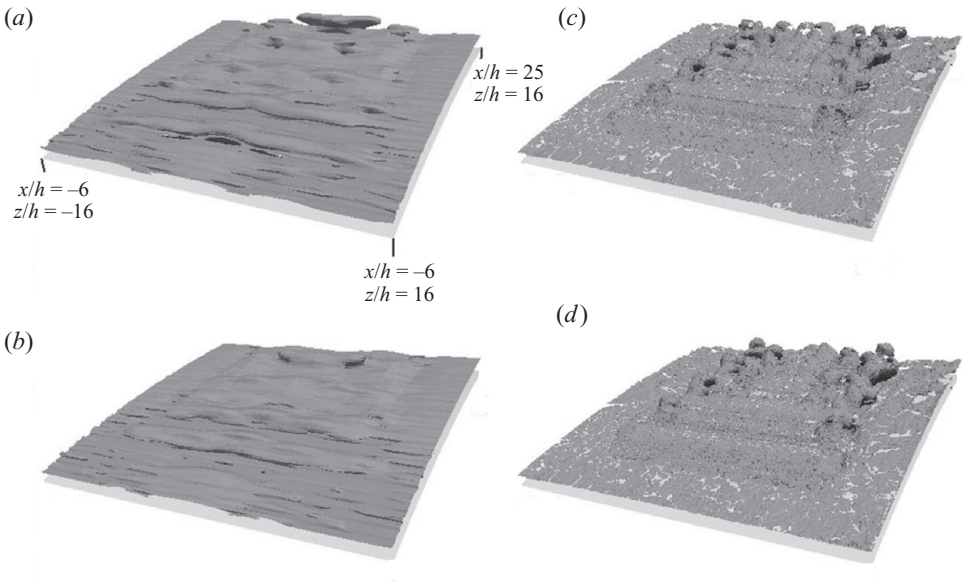


FIGURE 15. Iso-surfaces of the phase-averaged spanwise vorticity ($|\Omega_z|c/U_\infty = 30.5$); one in the clockwise sense (in light shade) and other in the counterclockwise sense (in dark shade). Experiments (a, b) and simulations (c, d) for an actuated case with $C_b = 0.4$ at two phases, $\phi = 120°$ (a, c) and 240° (b, d). In $(b–d)$, x/h and z/h values are the same as in (a).

CW vortex in the pair and resides in between two CW vortices issued in subsequent synthetic jet cycles. The reason for this is that the CCW vortex experiences a higher crossflow velocity during the jet cycle while it advects through a region outside the crossflow boundary layer. This behaviour leads to a train of counter-rotating vortices with diminishing strength that eventually lifts off the aerofoil surface. As shown later in figure 17, the CCW vortices of the synthetic jet are responsible for the lift-off mechanism.

Owing to the 3-D nature of the interaction between the synthetic jet and crossflow, one needs to measure/simulate the 3-D flow field. Figures 15 and 16 present iso-surfaces of the phase-averaged spanwise vorticity, based on experimental and numerical results, for $C_b = 0.4$ and $C_b = 1.2$, respectively. Two levels of spanwise vorticity are considered, which are equal in value but opposite in the directional sense, i.e. one is CW while the other is CCW. The non-dimensional value for these iso-surfaces is set to $|\Omega_z|c/U_\infty = 30.5$.

Figure 15 shows the phase-averaged flow field at $\phi = 120°$ and $\phi = 240°$ for the low blowing ratio case ($C_b = 0.4$). As can be seen, spanwise rollers, issued by the finite-span synthetic jet, are dominated by the clockwise structures near the jet slit. At downstream locations, organized secondary structures evolve, which can be clearly seen in numerical results in figures 15(c) and 15(d), whereas experimental data capture the same trend but with limited spatial resolution along the span due to the spacing between PIV planes. For this low blowing ratio case, the first two roller structures (issued in two subsequent synthetic jet cycles) are quasi-two-dimensional, except near the edges of the slit, where secondary structures form and perturb the rollers, leading to the formation of 3-D flow structures farther downstream. It is due to these flow structures and interactions that small waviness or a streak-like pattern is observed in the mean flow for the low blowing ratio case.

https://doi.org/10.1017/S0022112010005604 Published online by Cambridge University Press

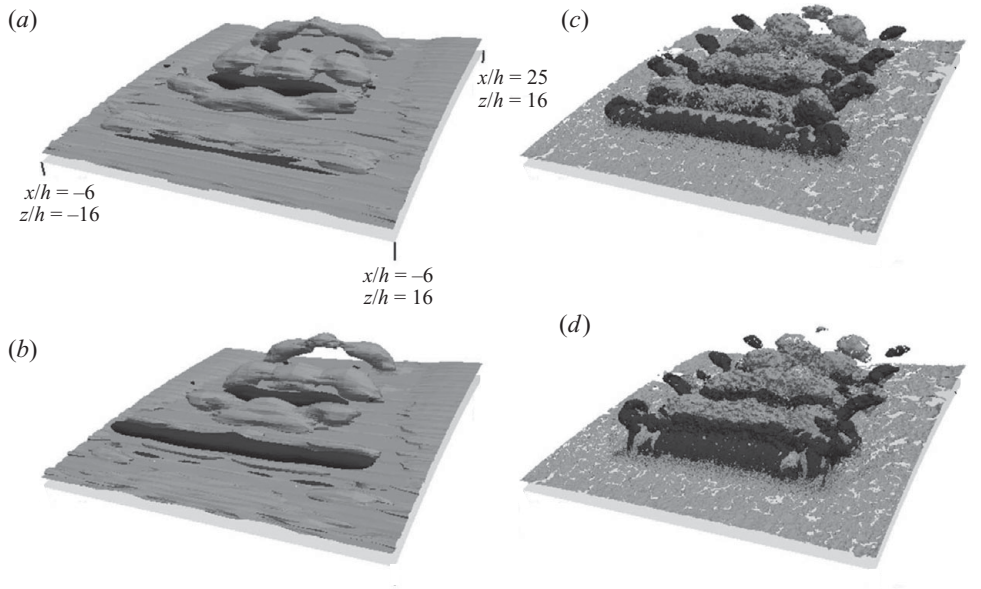


FIGURE 16. Iso-surfaces of the phase-averaged spanwise vorticity ($|\Omega_z|c/U_\infty = 30.5$); one in the clockwise sense (in light shade) and other in the counterclockwise sense (in dark shade). Experiments (a, b) and simulations (c, d) for an actuated case with $C_b = 1.2$ at two phases, $\phi = 120^\circ$ (a, c) and 240° (b, d). In $(b–d)$, x/h and z/h values are the same as in (a).

Next, figure 16 presents iso-surfaces of the phase-averaged spanwise vorticity for the high blowing ratio case ($C_b = 1.2$). In this case, the spanwise rollers are distinctly bigger and CCW vortex structure is present. One can see that these coherent vortical structures lose two-dimensionality, lift off the surface and possess less spanwise extent. All these observations are in accord with those discussed above.

To further understand the dynamics of vortical structures and their variation with the blowing ratio, experimental results are presented in figure 17 for three different levels of blowing ratios: $C_b = 0.4$ (in the low-level range), $C_b = 0.8$ (in the mid-level range) and $C_b = 1.2$ (in the high-level range). This figure presents phase-averaged spanwise vorticity across the centreplane of the jet at six different phases starting at the phase of 180°. This choice was made because the counter-rotating vortex pair formed in the current cycle is clearly evident at the jet slit. Grid lines are included in this figure to provide the location of the vortical structures at different phases. For the low blowing ratio case (figure 17*a–f*), the CW vorticity dominates, as the CCW vorticity portion of the synthetic jet is not able to overcome the CW vorticity of the crossflow boundary layer. Thus, periodic excitation due to the synthetic jet leads to a wave-like undulation in the crossflow boundary layer that is advected downstream with the main flow. As the blowing ratio is increased to $C_b = 0.8$ (figure 17*g–l*), the CCW vortex is visible near the synthetic jet orifice; vortical structure issued by the synthetic jet can be seen at the phase of 180° (when a counter-rotating vortical structure is clearly seen at $x/h = 0$, figure 17*g*). In a subsequent phase of 240° shown in figure 17(*h*), the current vortical structure issued by the synthetic jet is tilted due to the crossflow. At this phase, the CW vortical structure (immediately downstream of the orifice) remains near the surface while the CCW vortex rolls over it. In the next phase of 300° (figure 17*i*), the CCW vortex collides with the CW structure and splits it, and then resides between the two segments of the split CW structure. Note that

https://doi.org/10.1017/S0022112010005604 Published online by Cambridge University Press

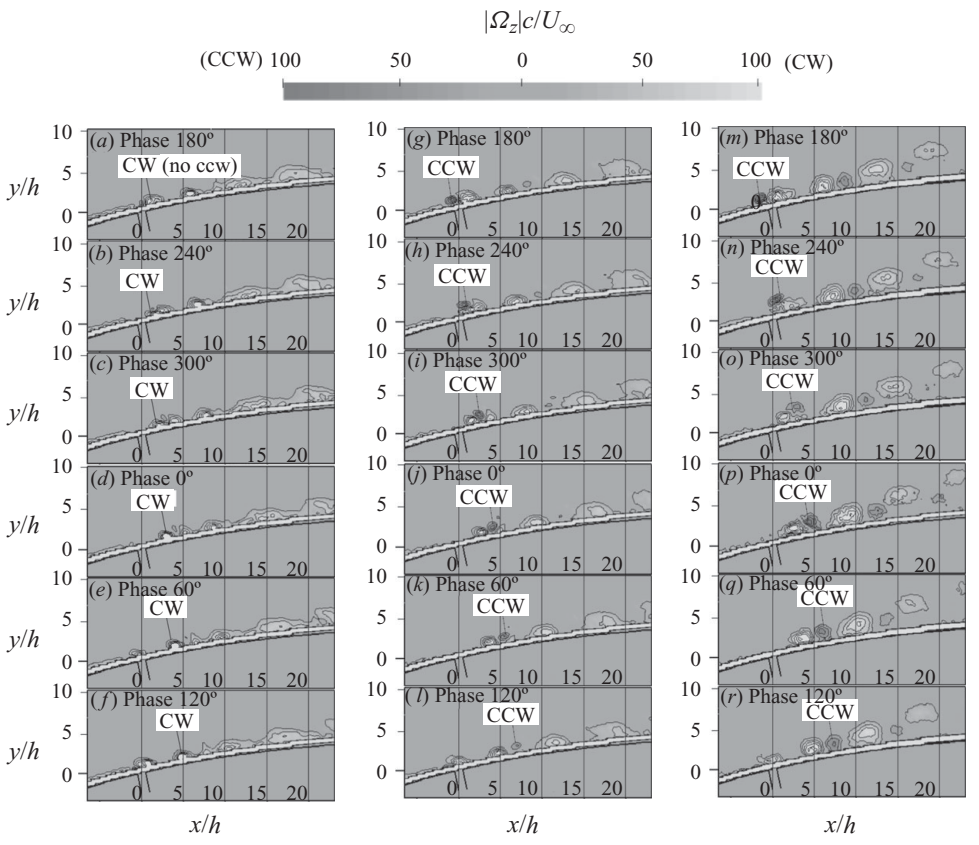


FIGURE 17. Phase-averaged spanwise vorticity based on experimental data on the centreplane for three actuated cases with $C_b = 0.4$ (*a–f*), 0.8 (*g–l*), and 1.2 (*m–r*). Six different phases (at every 60° starting from 180° at the topmost row) are considered to show temporal evolution and interactions of vortical structures.

at the phase of 0°, the front segment of the split CW structure is located at $x/h = 5$. By the phase of 60°, this segment is completely diffused while the lagging segment distinctly exists just before $x/h = 5$. Moreover, the CCW vortex becomes weaker, as can be seen in phases of 120° and 180° (i.e. in between $x/h = 5$ and $x/h = 10$). This cycle continues and the lagging segment of the CW vortical structure spreads and loses its coherence as it is advected downstream.

Figure 17(*m–r*) shows the evolution and advection of the vortical structures for the highest blowing ratio considered in this study ($C_b = 1.2$). At this blowing ratio, a counter-rotating vortex pair is issued from the jet orifice, which is titled by the crossflow (see the phase of 240°, figure 17*n*). In the next phase of 300°, the CCW structure overtakes the CW structure as it experiences a higher crossflow velocity and resides between subsequent CW structures. Furthermore, by the next jet cycle, the CCW structure due to its local upwash causes the downstream CW structure to lift off the surface, e.g. at the phase of 300° in figure 17(*o*), the CW structure from the previous cycle is lifted off (at $x/h = 15$).

In general, the flow field can be decomposed into three components: mean (time-averaged) flow, coherent (phase-locked) structures and turbulent (random) motions. To understand the importance of the coherent and random motions for different

https://doi.org/10.1017/S0022112010005604 Published online by Cambridge University Press

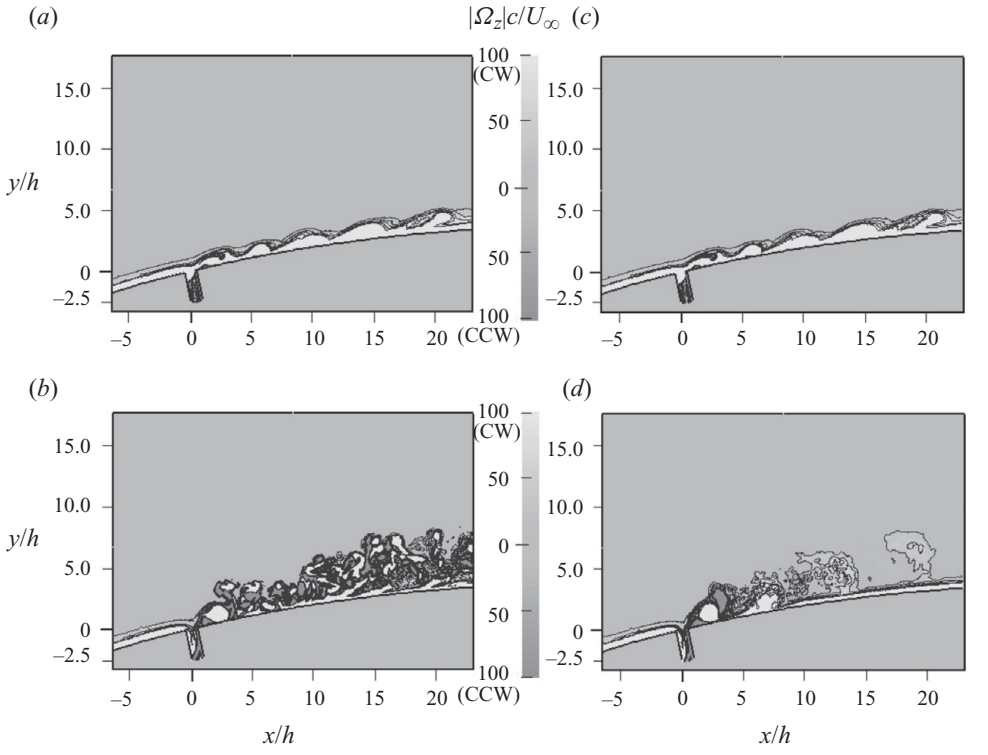


FIGURE 18. Spanwise vorticity, instantaneous (a,b) and phase-averaged (c,d), based on numerical data at the centreplane for two actuated cases with $C_b = 0.4$ (a,c) and 1.2 (b,d) at a phase of 240°. Shades are the same as in figure 13.

blowing ratios, instantaneous and phase-averaged spanwise vorticity fields were collected numerically and are compared in figures 18 and 20. Figure 18 shows data across the centreplane of the jet, whereas figure 20 presents the volumetric view in terms of iso-surfaces. In these figures, numerical data are presented for two actuated cases with $C_b = 0.4$ and $C_b = 1.2$. For the low blowing ratio case, the vortical structures observed in the instantaneous and phase-averaged flow fields (figures 18*a* and 18*c*, respectively) are nearly identical. For the higher blowing ratio case ($C_b = 1.2$), the situation is drastically different as the instantaneous field shows the presence of less coherent, turbulent motions, whereas the phase-averaged field, based on the jet cycle, exhibits coherent structures issued by the synthetic jet. Note that for the low blowing ratio case the synthetic jet is laminar while for the high blowing ratio case the jet falls within the turbulent regime, as was described (using flow visualization) by Chen *et al.* (2000). Moreover, owing to the presence of significant turbulent motions in the high blowing ratio, phase-averaging in simulations is based on samples over 350 cycles, which dramatically increases the cost of the simulations.

To further evaluate the range of physical scales present in the high blowing ratio case, the instantaneous velocity field at a point (i.e. time trace of velocity at a probe) was collected from the simulation. This collection was done for 350 jet cycles to compute energy spectra based on frequency. The probe was selected to be 10 slit widths downstream of the jet and 1 slit width above the aerofoil surface. This location was selected because the jet flow structures have transitioned to turbulence in this region. On the basis of the energy spectra (see figure 19), the inertial range is

https://doi.org/10.1017/S0022112010005604 Published online by Cambridge University Press

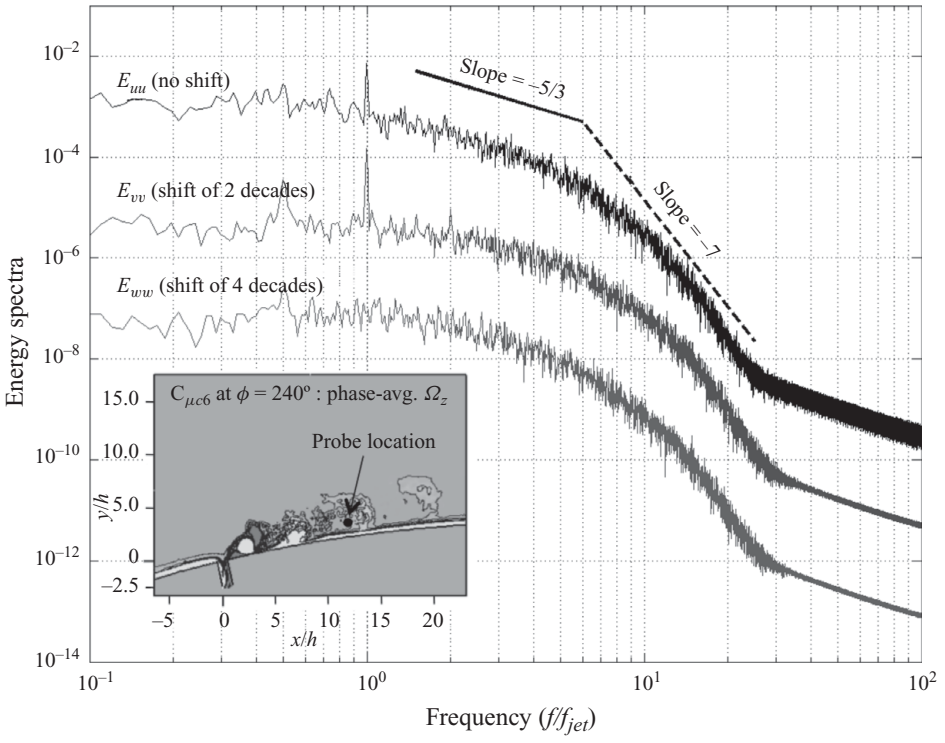


FIGURE 19. Energy spectra at a downstream probe location in the centreplane (shown in inset) for an actuated case with $C_b = 1.2$. Data were collected from simulations over 350 cycles.

found to span about half a decade and the presence of the dissipation range is clearly evident, which confirms the DNS resolution of the simulation. A similar observation was made by Kotapati *et al.* (2007) for a synthetic jet without a crossflow. Also, note that clear peaks are observed in the energy spectra at the jet frequency for both of the in-plane velocity components but, as expected, is absent in the spanwise component at this probe location in the centreplane (i.e. coherent structures of 2-D spanwise rollers are present near the centreplane).

Finally, figure 20 presents numerical data of the iso-surfaces of spanwise vorticity for the same two actuated cases at two phases of 120° and 240°. In each plot, instantaneous and phase-averaged fields are presented on the left- and right-halves of the span, respectively (lines in the mid-span depict the centreplane). As before, the case with $C_b = 0.4$ (figures 20*a* and 20*c*) shows nearly identical structures in the instantaneous and phase-averaged fields. Moreover, well-organized secondary structures are present. When the blowing ratio is increased to $C_b = 1.2$ (figure 20*b* and 20*d*), turbulent motions are dominant in the flow. It is because of the presence of such turbulent motions that the mean flow exhibits structures that appear to be merged together (as shown in figures 10*b* and 10*d* based on an iso-total velocity surface).

5. Conclusions

The interaction of a finite-span synthetic jet with a crossflow over a finite wing at a chord-based Reynolds number of 100 000 and a 0° angle of attack was studied experimentally and numerically. Experiments were conducted on a finite wing with

https://doi.org/10.1017/S0022112010005604 Published online by Cambridge University Press

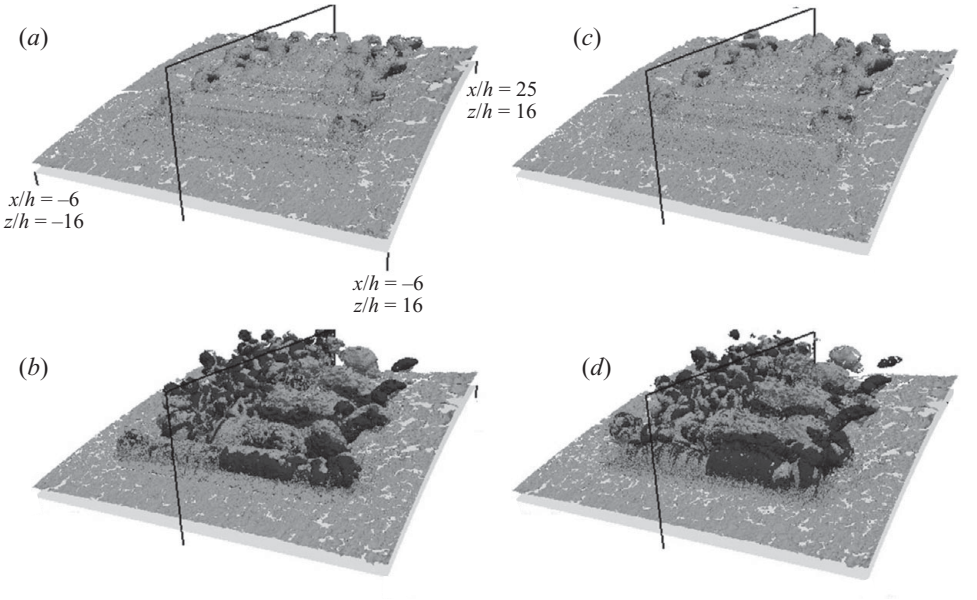


FIGURE 20. Iso-surfaces of the spanwise vorticity, instantaneous (left-half of the span in each case) and phase-averaged (right-half of the span), with equal but opposite values of $|\Omega_z|c/U_\infty = 30.5$ (the light shade has been used for the CW vorticity and the dark shade for the CCW vorticity). Numerical data are shown for two actuated cases with $C_b = 0.4$ (a, c) and 1.2 (b, d) at two phases, $\phi = 120°$ (a, b) and 240° (c, d). Lines in the mid-span depict the centreplane. In $(b–d)$, x/h and z/h values are the same as in (a).

a cross-sectional profile of NACA 4421, where a range of momentum coefficients were considered corresponding to six blowing ratios in the range from $C_b = 0.2$ to $C_b = 1.2$ (with an increment of 0.2). Numerical simulations of two actuated cases were performed, one corresponding to $C_b = 0.4$ (in the lower range where non-negligible effects due to synthetic jets were observed experimentally) and another corresponding to $C_b = 1.2$ (i.e. the highest actuation level). The numerical set-up matched not only the physical parameters (e.g. free-stream and blowing ratio) but also the physical dimensions (e.g. width and aspect ratio of jet slit, orientation and location of jet, and flow control cavity including slot and chamber).

A detailed comparison between experimental and numerical results was presented based on the time-averaged and phase-averaged flow fields at different locations, including along normal-to-the-surface lines and across the centreplane. Furthermore, since 3-D measurements were made experimentally, a volumetric comparison was also performed in a spanwise strip covering the full span of the synthetic jet. In all cases, good agreement was shown between the experimental measurements and numerical results but there were some limitations. For example, PIV data were not available very close to the surface whereas phase-averaged numerical data based on 350 jet cycles appeared to have limited statistical convergence in the high blowing ratio case. Furthermore, in the low blowing ratio case the resolution of experimental data in the span was limited, whereas in the high blowing ratio case there were discrepancies in velocity profiles immediately downstream of the jet exit and very near to the surface. Nonetheless, the joint investigation provided a detailed and complementary

https://doi.org/10.1017/S0022112010005604 Published online by Cambridge University Press

understanding of the flow interaction by taking advantage of the strength of each technique, e.g. long-time averaged data from experiments but high-resolution temporal and spatial data from simulations. Agreement on quantities that both can obtain was used to validate both the techniques.

In addition to a detailed comparison, 3-D interactions between the finite-span synthetic jet and crossflow were analysed based on time-averaged, phase-averaged and instantaneous flow fields. Experiments provided results for six different blowing ratios while simulations complemented detailed spatial and temporal data (as high-resolution 3-D instantaneous and averaged flow fields were available from current numerical simulations). Emphasis was placed on flow structures along with their interactions and evolution in the vicinity of the synthetic jet. It was found that in the low-momentum coefficient cases, 2-D spanwise rollers formed near the slit in each jet cycle; however, due to the finite span of the slit streamwise vortices developed at the edge of the slit. Furthermore, the crossflow accelerates around the edge of the slit and develops spanwise velocity components. As a result, the 2-D spanwise rollers are perturbed, leading to the formation of small and organized secondary flow structures farther downstream in the form of multiple distinct streak-like flow structures in the mean flow. On the other hand, in the high blowing ratio cases, turbulent vortical structures were dominant that lead to larger spanwise structures, or lobe-like patterns, in the mean flow, where three-dimensionalities were formed immediately downstream of the jet slit. Comparison of instantaneous and phase-averaged flow fields clearly showed the presence of significant turbulent motions (in contrast to the low blowing ratio case). In all cases the spanwise extent of the coherent structures reduced with downstream distance; the decrease was more for cases with higher blowing ratio. Similar flow patterns were observed in earlier studies on finite-span synthetic jets without a crossflow (e.g. Amitay & Cannelle 2006).

Spatial and temporal evolutions of flow structures were also studied with the help of cross-stream planes at different locations, and phase-averaged flow fields at six different phases. It was found that in low-range cases (with $C_b = 0.2$ and $C_b = 0.4$), well-organized structures existed in the form of multiple distinct streamwise-oriented secondary vortical structures. In the mid-blowing ratio range, combined features of the low range (near the slit) and high range (in downstream locations) were found and the pair of counter-rotating vortices issued in the same jet cycle collided with each other. In the high blowing ratio range, a train of counter-rotating coherent vortices existed that lifted off the surface as they advected downstream.

This work has been supported by the AFOSR, under grant number FA9550-08-1-0233, monitored by Drs J. Schmisseur and D. Smith. The support of the work done by Dr Onkar Sahni and Professor K. E. Jansen was provided by the NSF under grant OCI-0749152. Computing resources were provided by the NSF through TeraGrid resources at TACC (Ranger and Spur systems were used) and at NICS (the Kraken system was used). The numerical results presented in this article made use of the linear algebra library provided by ACUSIM Software Inc. We would also like to acknowledge that ParaView software provided by Kitware Inc. was used for visualization of the simulation data. The authors would like to thank undergraduate student K. Mossey for his tremendous help in organizing and processing of the experimental data. The authors would also like to acknowledge the insightful discussions provided by Y. Elimelech along with the help of undergraduate students D. Finigan and M. Lenihan.

https://doi.org/10.1017/S0022112010005604 Published online by Cambridge University Press

REFERENCES

Abbott, I. H. & von Doenhoff, A. E. 1959 *Theory of Wing Sections: Including a Summary of Airfoil Data*. Dover.

Amitay, M. & Cannelle, F. 2006 Evolution of finite-span synthetic jets. *Phys. Fluids* **18**, 054101.

Amitay, M. & Glezer, A. 2002*a* Role of actuation frequency in controlled flow reattachment over a stalled airfoil. *AIAA J.* **40**, 209–216.

Amitay, M. & Glezer, A. 2002*b* Controlled transients of flow reattachment over stalled airfoils. *Intl J. Heat Fluid Flow* **23**, 690–699.

Amitay, M. & Glezer, A. 2006 Flow transients induced on a 2D airfoil by pulse-modulated actuation. *Exp. Fluids* **40**, 329–331.

Amitay, M., Honohan, A., Trautman, M. & Glezer, A. 1997 Modification of the aerodynamic characteristics of bluff bodies using fluidic actuators. *AIAA Paper* 97-2004.

Amitay, M., Horvath, M., Michaux, M. & Glezer, A. 2001*a* Virtual aerodynamic shape modification at low angles of attack using synthetic jet actuators. *AIAA Paper* 2001-2975.

Amitay, M., Kibens, V., Parekh, D. E. & Glezer, A. 1999 Flow reattachment dynamics over a thick airfoil controlled by synthetic jet actuators. *AIAA Paper* 99-1001.

Amitay, M., Pitt, D. & Glezer, A. 2002*c* Separation control in duct flows. *J. Aircraft* **39**, 616–620.

Amitay, M., Smith, D. R., Kibens, V., Parekh, D. E. & Glezer, A. 2001*b* Modification of the aerodynamics characteristics of an unconventional airfoil using synthetic jet actuators. *AIAA J.* **39**, 361–370.

Bazilevs, Y., Calo, V. M., Cottrell, J. A., Hughes, T. J. R., Reali, A. & Scovazzi, G. 2007 Variational multiscale residual-based turbulence modeling for large eddy simulation of incompressible flows. *Comput. Meth. Appl. Mech. Engng* **197**, 173–201.

Cannelle, F. & Amitay, M. 2007 Transitory behavior of a finite-span synthetic jet. *Phys. Fluids* **19**, 094108.

Cater, J. E. & Soria, J. 2002 The evolution of round zero-net-mass-flux jets. *J. Fluid Mech.* **472**, 167–200.

Chatlynne, E., Rumigny, N., Amitay, M. & Glezer, A. 2001 Virtual aero-shaping of a Clark-Y airfoil using synthetic jet actuators. *AIAA Paper* 2001-0732.

Chen, F.-J., Yao, C., Beeler, G. B., Bryant, R. G. & Fox, R. L. 2000 Development of synthetic jet actuators for active flow control at NASA Langley. *AIAA Paper* 2000-2405.

Ciuryla, M., Liu, Y., Farnsworth, J., Kwan, C. & Amitay, M. 2007 Flight control using synthetic jets on a Cessna 182 model. *J. Aircraft* **44**, 642–653.

Crook, A., Sadri, A. M. & Wood, N. J. 1999 The development and implementation of synthetic jets for the control of separated flow. *AIAA Paper* 99-3176.

Crook, A. & Wood, N. J. 2001 Measurements and visualizations of synthetic jets. *AIAA Paper* 2001-0145.

Cui, J. & Agarwal, R. K. 2005 3D CFD validation of an axisymmetric jet in cross-flow (NASA Langley workshop validation: case 2). *AIAA Paper* 2005-1112.

Cui, J. & Agarwal, R. K. 2006 Three-dimensional computation of a synthetic jet in quiescent air. *AIAA J.* **44**, 2857–2865.

Dandois, J., Garnier, E. & Sagaut, P. 2006 Unsteady simulation of a synthetic jet in a crossflow. *AIAA J.* **44**, 225–238.

Farnsworth, J. A. N., Vaccaro, J. C. & Amitay, M. 2008 Active flow control at low angles of attack: Stingray unmanned aerial vehicle. *AIAA J.* **46**, 2530–2544.

Gallas, Q., Holman, R., Nishida, T., Carroll, B., Sheplak, M. & Cattafesta, L. 2003 Lumped element modeling of piezoelectric-driven synthetic jet actuators. *AIAA J.* **41**, 240–247.

Gilarranz, J. L., Traub, L. W. & Rediniotis, O. K. 2005 A new class of synthetic jet actuators. Part II. Application to flow separation control. *ASME J. Fluids Engng* **127**, 377–387.

Glezer, A. & Amitay, M. 2002 Synthetic jets. *Annu. Rev. Fluid Mech.* **34**, 503–529.

Glezer, A., Amitay, M. & Honohan, A. 2005 Aspects of low- and high-frequency actuation for aerodynamic flow control. *AIAA J.* **43**, 1501–1511.

Gordon, M. & Soria, J. 2002 PIV measurements of a zero-net-mass-flux jet in cross flow. *Exp. Fluids* **33**, 863–872.

Greenblatt, D. & Washburn, A. 2008 Influence of finite span and sweep on active flow control efficacy. *AIAA J.* **46**, 1675–1694.

https://doi.org/10.1017/S0022112010005604 Published online by Cambridge University Press

He, Y., Cary, A. W. & Peters, D. A. 2001 Parametric and dynamic modeling for synthetic jet control of a post-stall airfoil. *AIAA Paper* 2001-0733.

Ho, C.-M. & Huerre, P. 1984 Perturbed free shear layers. *Annu. Rev. Fluid Mech.* **16**, 365–422.

Iai, T., Motosuke M. & Honami, S. 2009 Vortex behavior of vertical and inclined synthetic jet in cross flow at low Reynolds number. *AIAA Paper* 2009-4178.

Jabbal, M. & Zhong, S. 2008 The near wall effect of synthetic jets in a boundary layer. *Intl J. Heat Fluid Flow* **29**, 119–130.

Jansen, K. E., Whiting, C. H. & Hulbert, G. M. 2000 A generalized-alpha method for integrating the filtered Navier–Stokes equations with a stabilized finite element method. *Comput. Meth. Appl. Mech. Engng* **190**, 305–319.

Kotapati, R. B., Mittal, R. & Cattafesta L. N, III. 2007 Numerical study of a transitional synthetic jet in quiescent external flow. *J. Fluid Mech.* **581**, 287–321.

Kral, L. D., Donovan, J. F., Cain, A. B. & Cary, A. W. 1997 Numerical simulation of synthetic jet actuators. *AIAA Paper* 97-1824.

Lee, C. Y. & Goldstein, D. B. 2002 Two-dimensional synthetic jet simulation. *AIAA J.* **40**, 510–516.

Maldonado, V., Farnsworth, J., Gressick, W. & Amitay, M. 2010 Active control of flow separation and structural vibrations of wind turbine blades. *Wind Energy*, **13**, 221–237.

Mallinson, S. G., Hong, G. & Reizes, J. A. 1999 Some characteristics of synthetic jets. *AIAA Paper* 99-3651.

Mallinson, S. G., Reizes, J. A., Hong, G. & Westbury, P. S. 2004 Analysis of hot-wire anemometry data obtained in a synthetic jet flow. *Exp. Therm. Fluid Sci.* **28**, 265–272.

Milanovic, I. M. & Zaman, K. B. M. Q. 2003 Synthetic jets in cross-flow. Part II. Jets from orifices of different geometry. *AIAA Paper* 2003-3715.

Milanovic, I. M., Zaman, K. B. M. Q. & Rumsey, C. L. 2005 An isolated circular synthetic jet in cross-flow at low momentum-flux ratio. *AIAA Paper* 2005-1110.

Mittal, R. & Rampunggoon, P. 2002 On the virtual aeroshaping effect of synthetic jets. *Phys. Fluids* **14**, 1533.

Mittal, R., Rampunggoon, P. & Udaykumar, H. S. 2001 Interaction of a synthetic jet with a flat-plate boundary layer. *AIAA Paper* 2001-2773.

Muppidi, S. & Mahesh, K. 2005 Study of trajectories of jets in crossflow using direct numerical simulations. *J. Fluid Mech.* **530**, 81–100.

Oster, D. & Wygnanski, I. 1982 The forced mixing layer between parallel streams. *J. Fluid Mech.* **123**, 91–130.

Parekh, D. E., Williams, S. P., Amitay, M., Glezer, A., Washburn, A. E., Gregory, I. M. & Scott, R. C. 2003 Active flow control on the Stingray UAV: aerodynamic forces and moments. *AIAA Paper* 2003-4002.

Pope, S. B. 2000 *Turbulent Flows*. Cambridge University Press.

Ravi, B. R., Mittal, R. & Najjar, F. M. 2004 Study of three-dimensional synthetic jet flowfields using direct numerical simulation. *AIAA Paper* 2004-0091.

Rizzetta, D. P., Stanek, M. J. & Visbal, M. R. 1999 Numerical simulation of synthetic-jet flowfields. *AIAA J.* **37**, 919–927.

Roberts, F. A. 1985 Effects of periodic disturbances on structure of mixing in turbulent shear layers and wakes. PhD thesis, California Institute of Technology.

Rumsey, C. L. 2004 Computation of a synthetic jet in a turbulent cross-flow boundary layer. *NASA/TM*-2004-213273.

Rumsey, C. L. 2009 Successes and challenges for flow control simulations. *Intl J. Flow Control* **1**, 1–27.

Saad, Y. & Schultz, M. H. 1986 GMRES: a generalized minimal residual algorithm for solving nonsymmetric linear systems. *SIAM J. Sci. Stat. Comput.* **7**, 856–869.

Sahni, O., Jansen, K. E., Shephard, M. S., Taylor, C. A. & Beall, M. W. 2008 Adaptive boundary layer meshing for viscous flow simulations. *Engng Comput.* **24**, 267–285.

Sahni, O., Mueller, J., Jansen, K. E., Shephard, M. S. & Taylor, C. A. 2006 Efficient anisotropic adaptive discretization of the cardiovascular system. *Comput. Meth. Appl. Mech. Engng* **195**, 5634–5655.

Sahni, O., Zhou, M., Shephard, M. S. & Jansen, K. E. 2009 Scalable implicit finite element solver for massively parallel processing with demonstration to 160k cores. In *Proc. 2009 Intl*

https://doi.org/10.1017/S0022112010005604 Published online by Cambridge University Press

Conf. High Performance Computing, Networking, Storage and Analysis (Supercomputing 2009), Portland, Oregon.

Sauerwein, S. C. & Vakili, A. D. 1999 An experimental study of zero-mass jets in crossflow. *AIAA Paper* 99-0668.

Schaeffler, N. W. & Jenkin, L. N. 2006 Isolated synthetic jet in crossflow: experimental protocols for a validation dataset. *AIAA J.* **44**, 2846–2856.

Seifert, A., Bachar, T., Koss, D., Shepshelovich, M. & Wygnanski, I. 1993 Oscillatory blowing: a tool to delay boundary-layer separation. *AIAA J.* **31**, 2052–2060.

Smith, B. L. & Glezer, A. 1998 The formation and evolution of synthetic jets. *Phys. Fluids* **10**, 2281–2297.

Smith, B. L. & Glezer, A. 2002 Jet vectoring using synthetic jets. *J. Fluid Mech.* **458**, 1–34.

Smith, D. R. 2002 Interaction of a synthetic jet with a crossflow boundary layer. *AIAA J.* **40**, 2277–2288.

Timor, I., Ben-Hamou, E., Guy, Y. & Seifert, A. 2007 Maneuvering aspects and 3D effects of active airfoil flow control. *Flow Turbulence Combust.* **78**, 429–443.

Timoshenko, S. & Woinowsky-Krieger, S. 1959 *Theory of Plates and Shells*. McGraw-Hill.

Trofimova, A. V., Tejada-Martinez, A. E., Jansen, K. E. & Lahey, R. T. 2009 Direct numerical simulation of turbulent channel flows using a stabilized finite element method. *Comput. Fluids* **38**, 924–938.

Whiting, C. H. & Jansen, K. E. 2001 A stabilized finite element formulation for the incompressible Navier–Stokes equations using a hierarchical basis. *Intl J. Numer. Meth. Fluids* **35**, 93–116.

Wu, D. K. L. & Leschziner, M. A. 2009 Large-eddy simulations of circular synthetic jets in quiescent surroundings and in turbulent cross-flow. *Intl J. Heat Fluid Flow* **30**, 421–434.

Wygnanski, I. 2000 Some new observations affecting the control of separation by periodic excitation. *AIAA Paper* 2000-2314.

Xia, H. & Qin, N. 2005 Detached-eddy simulation for synthetic jets with moving boundaries. *Mod. Phys. Lett.* B **19**, 1429–1434.

Yao, C., Chen, F. J., Neuhart, D. & Harris, J. 2004 Synthetic jet flow field database for CFD validation. *AIAA Paper* 2004-2218.

You, D. & Moin, P. 2008 Active control of flow separation over an airfoil using synthetic jets. *J. Fluids Struct.* **24**, 1349–1357.

Zaman, K. B. M. Q. & Milanovic, I. M. 2003 Synthetic jets in cross-flow. Part 1. Round jet. *AIAA Paper* 2003-3714.

Zhou, J. & Zhong, S. 2009 Numerical simulation of the interaction of a circular synthetic jet with a boundary layer. *Comput. Fluids* **38**, 393–405.

https://doi.org/10.1017/S0022112010005604 Published online by Cambridge University Press